NOZZLEPY

NozzlePy Documentation and Mathematical Background

Based on the Bachelor's Thesis submitted to the Chair of Space Mobility and Propulsion at Technical University of Munich with the Title - Expansion nozzle design and optimisation for an H2/O2 Water Electrolysis Propulsion Spacecraft Thruster -

Version 1.1

Created by Philipp Matthiass

Contents

List of Figures

List of Tables

List of Symbols

General Symbols

$\dot{m}$	$[g/s]$	mass flow rate
a	$[m/s]$	speed of sound
A	$[mm^2]$	area
A_t	$[mm^2]$	area at nozzle throat
c	$[J/kgK]$	specific heat capacity
C_f	[-]	thrust coefficient
d_{opt}	[-]	optimization depth
F	$[N]$	thrust
F_b	$[N]$	external force
F_s	$[N]$	shear force
h	$[J]$	static enthalpy
I_{sp}	$[s]$	specific impulse
Ma	[-]	Mach number
Ma_{IVL}	[-]	Mach number at initial value line
n_v	[-]	number of variables per optimization step
n_l	[-]	number of initial calculation points - resolution of characteristic mesh
p	$[Pa]$	static pressure
R	$[J/kgK]$	specific gas constant
r_{arc}	$[mm]$	radius of circular arc at nozzle throat
r_t	$[mm]$	radius of nozzle throat
Re_s	[-]	Reynolds number along nozzle wall contour
res_p	[-]	resolution of parabola
S	$[K]$	Sutherland constant

s	$[mm]$	distance along nozzle wall contour
T	$[K]$	temperature
T_0	$[K]$	reference temperature
u	$[m/s]$	flow velocity in axial direction
V	$[m/s]$	total flow velocity
v	$[m/s]$	flow velocity in radial direction
x	$[mm]$	axial position
y	$[mm]$	radial position
y_t	$[mm]$	throat radius for initial value line

Greek Symbols

β	$[°]$	diverging half angle
δ^*	$[mm]$	boundary layer displacement thickness
δ_{99}	$[mm]$	99% boundary layer
γ	[-]	isentropic exponent
κ	[-]	heat capacity ratio
λ	$[°]$	slope of characteristic lines
μ	$[°]$	Mach angle
μ_0	$[Pa \cdot s]$	reference dynamic viscosity
ν	$[m^2/s]$	kinematic viscosity
ρ	$[g/m^3]$	density
ρ_t	$[mm]$	throat curvature radius for initial value line
τ_w	$[Pa]$	shear stress at nozzle wall
θ	$[°]$	flow angle with respect to axial direction
θ_{max}	$[°]$	maximal nozzle contour angle
ε	[-]	Euler error tolerance

Subscripts

$\square_+$	quantity on left-running characteristic
$\square_-$	quantity on right-running characteristic
$\square_0$	total stagnation property

$\square_1$	initial point on right-running characteristic
$\square_2$	initial point on left-running characteristic
$\square_4$	solution point
$\square_\infty$	quantity at ambient condition
$\square_{cc}$	quantity at combustion chamber condition
$\square_e$	quantity at nozzle exit plane
$\square_p$	quantity at constant pressure
$\square_s$	isentropic quantity

Superscripts

$\square^*$	nozzle throat
$\square^c$	Euler corrector
$\square^p$	Euler predictor

Special Symbols

∇	Nabla-operator
C_+	left-running characteristic line
C_-	right-running characteristic line

Abbrevations

DXF	Drawing Exchange Format
IVL	Initial Value Line
MoC	Method of Characteristics
TIC	Truncated Ideal Contour
TOP	Thrust Optimized Parabola

1. Introduction

1.1. Combustion chamber nozzles

Expansion nozzles are an essential part of any combustion chamber, as they accelerate the combusted gases to supersonic velocities, significantly influencing the thrust and efficiency of its engine. A traditional thruster nozzle is based on the De Laval nozzle, proposed by Gustav De Laval in 1890 [1]. In principle, it can be divided into two sections. The initial converging section accelerates the subsonic flow to its sonic velocity as it decreases its static pressure and temperature. The now choked flow cannot gain velocity by minimizing the nozzle cross-section any further; its Mach number is limited to unity at the throat. To further increase the velocity of the flow beyond Mach 1, the nozzle requires a successive diverging section, which decreases static pressure and temperature and accelerates the flow in the supersonic regime, as can be seen in figure (1.1). A more in-depth mathematical elucidation is provided in chapter (2).

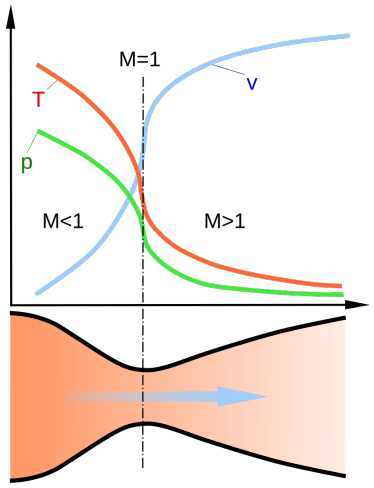

Figure 1.1.: Flow properties in a De Laval nozzle [2]

In the scope of this document, the nozzle is defined as the geometry directly downstream of the narrowest cross-section of the combustion chamber.

1.2. Document structure

The semi-analytical calculation of supersonic flow fields in combustion chamber nozzles and the corresponding evaluation of nozzle efficiency has, to date, been primarily applied to ideal nozzle contours. NozzlePy extends the Method of Characteristics, originally developed for the design of ideal expansion nozzles, to a similarly prevalent, non-ideal parabolic geometry by applying the mathematical background

of the ideal contour calculation to novel geometries using numerical tools developed in this work. Furthermore, it seeks to compare the resulting nozzle efficiencies of these distinct geometries, with particular emphasis on the influence of viscous and wall friction effects on overall performance. In order to give a detailed insight into the theoretical background and practical application, the document will be divided into six chapters.

Following the introduction, chapter two presents the fundamentals of one-dimensional rocket nozzle theory as the basis for further investigations. In chapter three, the theoretical background to calculations of the supersonic flow field is presented, as well as the practical application of the underlying Method of Characteristics (MoC) for the developed numerical tools. Chapter four focuses on the generation of nozzle contours, where various contour design approaches, such as Truncated Ideal Contour (TIC), RAO, Thrust Optimized Parabola (TOP), and TICTOP are assessed regarding their respective limitations. In chapter five, the performance of the generated contours is analyzed with respect to thrust, thrust coefficient, and specific impulse. Furthermore, ideal and real losses are investigated, emphasizing boundary layer effects and their influence on nozzle efficiency and geometry. This is calculated by a separate computational tool for the different contour methods TIC and TOP. Finally, chapter six describes the optimization program, designed to improve nozzle performance by systematically varying key design parameters.

2. Expansion nozzle fundamentals

In order to fully understand the flow phenomena of a converging-diverging nozzle, this chapter will provide an overview of the fundamental principles of such flow. The theoretical background is developed from the quasi-one-dimensional equations of compressible gas dynamics, which govern the relations between area change, velocity, and Mach number. Since this topic is rather elemental, it is well documented in many fluid- and thermodynamics textbooks, for example, Anderson [3], which is used as a foundation for this chapter.

2.1. Governing equations for quasi-one-dimensional flow

An expansion nozzle can be modeled as a duct with a varying cross-sectional area A(x). In addition, the flow can be assumed to be quasi-one-dimensional, which states that although the flow is three-dimensional in reality, the geometrical variation of a cross section is small compared to the variation along the nozzle axis. Under this assumption, the flow variables are treated as uniform across each cross section and depend only on the axial coordinate x. Figure (2.1) gives an overview of such an incremental cross-sectional control volume. This property simplifies the governing flow equations as follows:
The continuity equation can be stated as:

$$\dot{m} = \rho u A = constant, \tag{2.1}$$

where $\dot{m}$ denotes the fluid mass flow rate, ρ the flow density, u its velocity, and A the cross-sectional area. The momentum equation is expressed by:

$$pA + \rho u^2 A + pdA = (p + dp)(A + dA) + (\rho + d\rho)(u + du)^2(A + dA), \tag{2.2}$$

where additionally, p resembles the static pressure.

All products of differentials, such as $dpdA$, and $d\rho(du)^2$, can be ignored as they are small compared to the rest of the flow properties. Combining Equation (2.1) and the now simplified (2.2), yields the differential form of the momentum equation [3]:

$$dp = -\rho u \cdot du \tag{2.3}$$

Additionally, the first law of thermodynamics for adiabatic flow yields the energy equation:

$$h + \frac{u^2}{2} = h_0 = constant \tag{2.4}$$

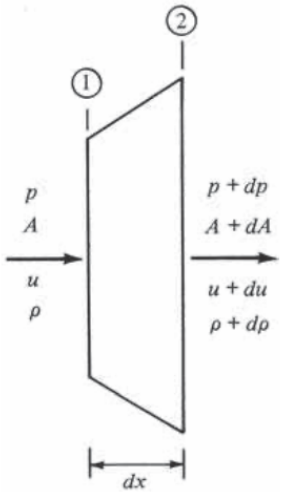

Figure 2.1.: Incremental control volume in expansion nozzle, Anderson [3], p.697, Fig. 10.8

Here, h is the static enthalpy and h_0 the total stagnation enthalpy of the fluid. The relation shows that in adiabatic, inviscid flow, the stagnation enthalpy remains constant. As the fluid can be treated as a calorically perfect gas, the thermodynamic relations are:

$$h = c_p T = \frac{\gamma}{\gamma - 1} RT, \qquad a^2 = \gamma RT, \tag{2.5}$$

where c_p denotes the specific heat capacity at constant pressure, T the local flow temperature, γ the ratio of specific heats, R the specific gas constant, and a the local speed of sound. Equations (2.1) through (2.5) together provide the fundamental mathematical framework from which the nozzle flow relations are derived.

2.2. Differential governing equations

To connect the change in area of the nozzle to changes in velocity, it is necessary to differentiate the continuity equation (2.1):

$$\frac{d\rho}{\rho} + \frac{du}{u} + \frac{dA}{A} = 0 \tag{2.6}$$

Equation (2.6) shows that variations in density, velocity, and area are not independent but are linked by the requirement of mass conservation. Similarly, Euler's momentum equation (2.3) can be written as:

$$\frac{dp}{\rho} = -u \cdot du \tag{2.7}$$

For isentropic flow, the thermodynamic identity holds:

$$\frac{dp}{d\rho} = a^2, \tag{2.8}$$

which, when combined with (2.7), yields:

$$\frac{d\rho}{\rho} = -\frac{u}{a^2}du \tag{2.9}$$

Introducing the Mach number of a fluid as $Ma = \frac{u}{a}$, equation (2.9) can be written as:

$$\frac{d\rho}{\rho} = -Ma^2\frac{du}{u} \tag{2.10}$$

Substituting Equation (2.10) into the continuity relation (2.6) and simplifying it gives the area-velocity relation:

$$\frac{dA}{A} = (Ma^2 - 1)\frac{du}{u} \tag{2.11}$$

Equation (2.11) is an important result in nozzle theory, as it shows the counterintuitive behavior of compressible flows compared to incompressible flows. For subsonic flows with a Mach number of ($Ma < 1$), acceleration ($du > 0$) requires a decrease in area, which is achieved by the converging section of the expansion nozzle. At sonic condition ($Ma = 1$), equation (2.11) demands a local extremum of the area ($\frac{dA}{A} = 0$). This is physically described as the throat of the nozzle, its narrowest cross-section. To now increase the velocity of the flow in the supersonic regime ($Ma > 1$) an increase in area is required. This resembles the distinctive diverging duct.

2.3. Area-Mach relation and isentropic flow properties

In order to gain exact information about the behavior of the nozzle geometry, depending on the flow properties, the continuity equation (2.1) can be set into relation between the throat ($A^*, Ma = 1$) and an arbitrary section in the nozzle by the following equation:

$$\frac{A}{A^*} = \frac{\rho^*}{\rho}\frac{a^*}{u} = \frac{\rho^*}{\rho_0}\frac{\rho_0}{\rho}\frac{a^*}{u} \tag{2.12}$$

The stagnation density - density relation for $Ma = 1$ for isentropic flow is defined by one of the fundamental equations of thermodynamics:

$$\frac{\rho^*}{\rho_0} = \left(\frac{2}{\gamma+1}\right)^{\frac{1}{\gamma-1}} \tag{2.13}$$

Similarly, the isentropic relation for the flow density at any arbitrary point in the nozzle can be defined as:

$$\frac{\rho}{\rho_0} = \left(1 + \frac{\gamma-1}{2}Ma^2\right)^{-\frac{1}{\gamma-1}} \tag{2.14}$$

Substituting these relations into equation (2.12), we can determine the Area-Mach relation:

$$\frac{A}{A^*} = \frac{1}{Ma}\left[\frac{2}{\gamma+1}\left(1 + \frac{\gamma-1}{2}Ma^2\right)\right]^{\frac{\gamma+1}{2(\gamma-1)}} \tag{2.15}$$

Equation (2.15) allows for the determination of the Mach number as a function of the area ratio $\frac{A}{A^*}$. It also reveals that each area ratio corresponds to two possible solutions: one subsonic and one supersonic. Through this equation, the Mach number can be determined for a given quasi-one-dimensional nozzle

geometry. Once, $Ma(x)$ is calculated, the remaining flow properties can be calculated via the isentropic relations, similar to the density ratio from Equation (2.14).
The pressure ratio is defined as:

$$\frac{p}{p_0} = \left(1 + \frac{\gamma - 1}{2} Ma^2\right)^{-\frac{\gamma}{\gamma - 1}}, \tag{2.16}$$

and the temperature ratio as:

$$\frac{T}{T_0} = \left(1 + \frac{\gamma - 1}{2} Ma^2\right)^{-1} \tag{2.17}$$

These equations describe how the static pressure and temperature decrease monotonically as the flow accelerates from subsonic to supersonic speeds in a well-expanded nozzle. They will be applied to determine the fluid properties in the supersonic regime in the following chapters.

2.4. Choking and limitation of mass flow

An essential feature of expansion nozzle operation is the choking of the flow at the throat, where the maximum mass flux is reached. The corresponding mass flow rate is:

$$\dot{m} = \rho^* a^* A^*. \tag{2.18}$$

Combining Equations (2.5), (2.13), (2.16) and (2.18) yields the mass flux at the nozzle throat in terms of reservoir conditions:

$$\dot{m} = p_0 A^* \sqrt{\frac{\gamma}{R T_0}} \left(\frac{2}{\gamma + 1}\right)^{\frac{\gamma + 1}{2(\gamma - 1)}} \tag{2.19}$$

Equation (2.19) shows that the maximum mass flow rate depends only on the stagnation pressure p_0, stagnation temperature T_0, throat area A^*, R, and γ. Once the flow is choked, further reduction of the pressure downstream cannot increase $\dot{m}$. The flow upstream of the throat becomes insensitive to downstream conditions, as flow information travels at the sonic velocity of the fluid, which is reached at the nozzle throat.

With the equations derived in this chapter, one can calculate the supersonic flow properties of a quasi-one-dimensional converging-diverging nozzle with isentropic flow. In addition, it is possible to calculate the optimal throat area for a given mass flux by rearranging equation (2.19). However, this approach has grave limitations. Firstly, the actual supersonic flow in an axisymmetric expansion nozzle shows strictly two-dimensional behavior, as the density, pressure, temperature, and velocity vary across each nozzle cross-section. Secondly, this method only captures the mean behavior of the flow; it does not provide the exact contour required to achieve ideal expansion.

3. Two-dimensional nozzle flow

While the quasi-one-dimensional method presented in the previous chapter explains the fundamental physical behavior of converging–diverging nozzles, it cannot prescribe the exact nozzle contour required to achieve a uniform, shock-free supersonic flow at the exit. In reality, the irrotational flow in the divergent section of an axisymmetric nozzle is inherently two-dimensional, governed not only by axial variations in area but also by transverse gradients in velocity, pressure, and temperature. To design nozzles that expand gases isentropically to supersonic speeds, a more refined theoretical tool is required.

The Method of Characteristics (MoC) provides the mathematical background of such a tool. The calculation of hyperbolic partial differential equations by using the MoC can be traced back to Joseph-Louis Lagrange, who published a general method of transferring partial differential equations into quasi-linear differential equations and solving them in 1779 [4]. However, it was not applied to supersonic flow calculations until 1929 [5], as Prandtl and Busemann utilized the MoC to calculate supersonic flow parameters and optimize nozzle geometries.

The Method of Characteristics offers a systematic procedure to solve two-dimensional, inviscid, supersonic flow fields. Its central idea is that the governing equations of compressible fluid motion can be transformed into compatibility relations along special families of curves in the flow field, called characteristic lines. Along these lines, information propagates in a well-defined manner, and the partial differential equations reduce to ordinary differential equations, which can be integrated more directly.

The following chapter will therefore introduce the theoretical foundations of the Method of Characteristics as applied to supersonic flow. After deriving the governing equations, its linearization will be established, followed by an outline on the initial condition of the supersonic flow in the nozzle.

3.1. Theoretical background of the Method of Characteristics

The calculations presented in this chapter are based on the theory proposed by Zucrow and Hoffman [6],[7]. Just as the quasi-one-dimensional nozzle theory from chapter (2), the Method of Characteristics is based on the continuity and momentum equations. However, the simplification of treating the flow variables as uniform across the cross-section of the contour is now invalid. Hence, the equations are to be utilized in their partial differential form. The general continuity equation yields:

$$\frac{\partial \rho}{\partial t} + \nabla \cdot (\rho \mathbf{V}) = 0, \tag{3.1}$$

where ∇ represents the Nabla-operator and V denotes the flow velocity. The momentum equation is:

$$\rho\left(\frac{\partial \mathbf{V}}{\partial t} + (\mathbf{V}\cdot\nabla)\mathbf{V}\right) + \nabla p - \rho F_b - dF_s = \mathbf{0}, \tag{3.2}$$

where F_b is any external force on the fluid, such as gravity, and F_s is the internal shear force due to flow viscosity. A set of assumptions is declared for the calculations:

- the fluid is steady ($\frac{\partial()}{\partial t} = 0$), adiabatic and inviscid ($dF_s = 0$)
- there are no internal heat sources in the flow
- neither volumetric force nor external work is considered ($F_b = 0$)
- the flow is isentropic
- the flow is irrotational and axisymmetric
- the propellants in the combustion chamber are treated as an ideal gas with constant temperature
- the fluid is modeled as a calorically perfect gas, meaning that the isentropic exponent γ is constant

As of the first assumption, the energy equation does not provide any additional independent information. The total enthalpy is conserved along a streamline, and the energy equation is therefore implicitly satisfied. The above derived properties reduce equations (3.1) and (3.2) to the following relations:

$$\nabla\cdot(\rho\mathbf{V}) = 0 \tag{3.3}$$

and

$$\rho\left((\mathbf{V}\cdot\nabla)\mathbf{V}\right) + \nabla p = \mathbf{0} \tag{3.4}$$

For an isentropic flow, the sonic velocity can be defined as

$$a^2 = \left(\frac{\partial p}{\partial \rho}\right)_s = \gamma\,\frac{p}{\rho}, \tag{3.5}$$

with s as the constant entropy. Making use of this relation, we can alter the form of the continuity equation:

$$(\mathbf{V}\cdot\nabla)p + \rho a^2\,\nabla\cdot\mathbf{V} = 0 \tag{3.6}$$

Combining Equations (3.2) and (3.6), and rewriting the result in dependence on the two-dimensional coordinates of the flow yields the gas dynamic equation:

$$(u^2 - a^2)\frac{\partial u}{\partial x} + (v^2 - a^2)\frac{\partial v}{\partial y} + 2uv\frac{\partial u}{\partial y} - \frac{a^2 v}{y} = 0 \tag{3.7}$$

It can be described as a combination of the continuity and momentum equations, coupling the streamline acceleration and turning to the compressibility of the flow. In order to fulfill the assumption of axisymmetrical, irrotational flow, the following equation holds true:

$$\frac{\partial u}{\partial y} - \frac{\partial v}{\partial x} = 0 \tag{3.8}$$

Equation (3.7) and (3.8) form a system of two partial differential equations, which can be combined, factorized with the arbitrary variables σ_1 and σ_2, and rearranged to:

$$\sigma_1(u^2 - a^2)\left(\frac{\partial u}{\partial x} + \frac{\sigma_1(2uv) + \sigma_2}{\sigma_1(u^2 - a^2)}\frac{\partial u}{\partial y}\right) - \sigma_2\left(\frac{\partial v}{\partial x} + \frac{\sigma_1(v^2 - a^2)}{-\sigma_2}\frac{\partial v}{\partial y}\right) - \frac{\sigma_1 a^2 v}{y} = 0 \tag{3.9}$$

This partial differential equation describes the motion of the fluid in an axisymmetric flow under given assumptions. However, it is not possible to solve this equation explicitly [6]. Therefore, the Method of Characteristics modulates this equation.

Supersonic flow, in contrast to subsonic flow, underlies the hyperbolic nature of the governing equations. Disturbances in the flow only alter it in a limited region, not throughout the complete flow field. This region is indicated as the region of influence of point A in figure (3.1).

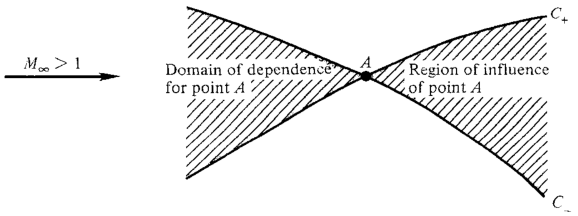

Figure 3.1.: Domain of dependence and region of influence of point A. [8], p.397, Fig. 11.12

This region is bound by the characteristic lines of point A, with C_+ and C_- describing the left- and right-running characteristics, respectively. Flow information of fluid particles in the region of influence is unable to propagate across these characteristic lines. This restricted communication makes the method of characteristics possible since it allows local solutions, derived from equation (3.9), to be propagated directly along the characteristic lines. Characteristics are defined as curves with the slope:

$$\lambda = \frac{\sigma_1(2uv) + \sigma_2}{\sigma_1(u^2 - a^2)} \qquad \text{and} \qquad \lambda = \frac{\sigma_1(v^2 - a^2)}{-\sigma_2} \tag{3.10}$$

In addition, every variable of equation (3.9) must be continuous [6], which yields the total differential of the velocities u and v:

$$\frac{du}{dx} = \frac{\partial u}{\partial x} + \frac{dy}{dx}\frac{\partial u}{\partial y} \qquad \text{and} \qquad \frac{dv}{dx} = \frac{\partial v}{\partial x} + \frac{dy}{dx}\frac{\partial v}{\partial y} \tag{3.11}$$

Since the MoC is only applicable to the characteristic lines, defined by equations (3.10), term $\frac{dy}{dx}$ of equations (3.11) describes exactly the slopes of the characteristics. Therefore, equation (3.11) can be rewritten as:

$$\frac{du}{dx} = \frac{\partial u}{\partial x} + \lambda\frac{\partial u}{\partial y} \qquad \text{and} \qquad \frac{dv}{dx} = \frac{\partial v}{\partial x} + \lambda\frac{\partial v}{\partial y} \tag{3.12}$$

Inserting equation (3.10) into equation (3.12) and consequently into equation (3.9) yields:

$$\sigma_1(u^2 - a^2)du - \sigma_2 dv - \left(\frac{\sigma_1 a^2 v}{y}\right) dx = 0 \tag{3.13}$$

In order to solve the still unknown variables σ_1 and σ_2, equations (3.10) can be transformed into a linear equation system:

$$\begin{bmatrix} (u^2 - a^2)\lambda - 2uv & -1 \\ (v^2 - a^2) & \lambda \end{bmatrix} \begin{pmatrix} \sigma_1 \\ \sigma_2 \end{pmatrix} = 0 \tag{3.14}$$

Since the trivial solution of $\sigma_1 = \sigma_2 = 0$ does not provide additional information, the matrix determinant of equation (3.14) must be set equal to unity:

$$(u^2 - a^2)\lambda^2 - 2uv\lambda + (v^2 - a^2) = 0 \tag{3.15}$$

Solving equation (3.15) for λ and manipulating the result by means of trigonometric functions reveals a new definition for the slope of the characteristics:

$$\lambda_\pm = \left(\frac{dy}{dx}\right)_\pm = \frac{uv \pm a^2\sqrt{Ma^2 - 1}}{u^2 - a^2} = \tan(\theta \pm \mu), \tag{3.16}$$

where θ denotes the flow angle with respect to the initial flow axis, and μ is the current Mach angle of the flow, as shown in figure (3.2).

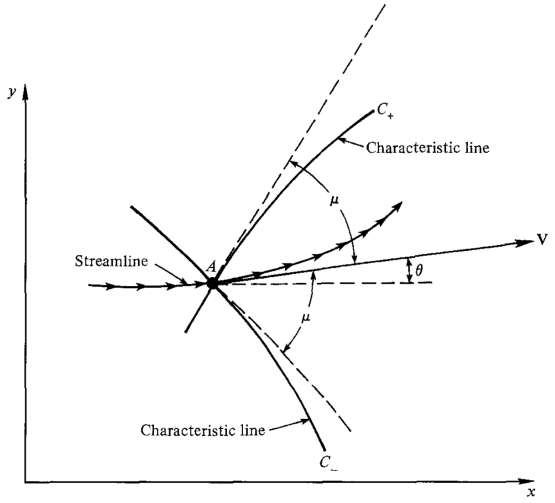

Figure 3.2.: Left- and right-running characteristics of point A. [8], p.390, Fig. 11.8

Equation (3.16) is called the characteristic equation. Now, that λ is known, substituting either equation of (3.10) into equation (3.13) yields the compatibility equation:

$$(u^2 - a^2)du_\pm + (2uv - (u^2 - a^2)\lambda_\pm)dv_\pm - \left(\frac{a^2 v}{y}\right) dx_\pm = 0. \tag{3.17}$$

The relations (3.16) and (3.17) are the two fundamental equations of the method of characteristics.

3.2. Linearization of the MoC

The flow properties at a certain position in the supersonic flow field are defined by the point's position- and velocity- vector:

$$\begin{pmatrix} x \\ y \end{pmatrix}, \begin{pmatrix} u \\ v \end{pmatrix} \tag{3.18}$$

These four variables can be solved by evaluating the four equations (3.16) and (3.17). However, additional flow information cannot be gained by only one input condition. The solution of these equations for the same input parameters for both the left- and right-running characteristics yields only the trivial solution of the input point itself. Per definition, the characteristic lines, originating from the same point, only have one intersection at that originating point (e.g. point A of figure (3.2)).
For an initial condition of two points, this problem no longer occurs, as the C_+ and C_- characteristics of the initial points, respectively, intersect at a third point. The properties (3.18) at the intersection point can then be derived. This is valid for the initial points 1 and 2 to be positioned anywhere within the flow field but on the same characteristic. Figure (3.3) shows such a scenario, as points 1 and 2 provide the initial flow data and point 4 is calculated via MoC.

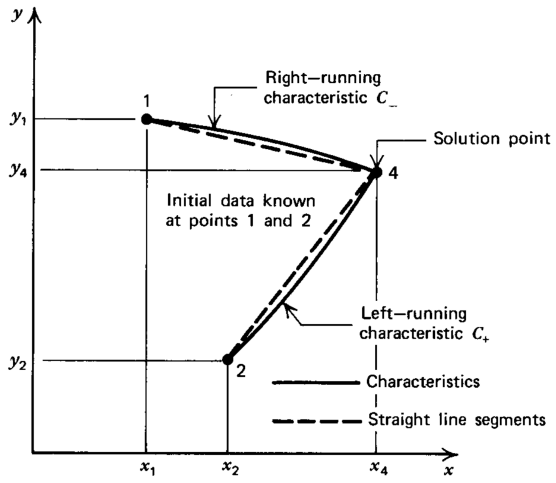

Figure 3.3.: Characteristic crossing for applying the Method of Characteristic, [6], p.598, Fig. (12.9)

This section focuses on the exact linearized calculation of the flow properties at an additional point in the flow field. The notation is in accord with Figure (3.3): The initial points are labeled $()_1$ and $()_2$ respectively, and the solution point is numbered $()_4$.

3.2.1. Interior points

The general application of the MoC is the calculation of the flow parameters of a point downstream of the initial conditions, independent of symmetry or physical boundary conditions. The four properties (3.18) of point 4 are calculated by the characteristic- and compatibility equations of the right running characteristic of point 1 and the left running characteristic of point 2. By integration and rearranging of

equations (3.16), the following equations for the C_+ and C_- characteristic yield:

$$y_4 - \lambda_+ x_4 = y_2 - \lambda_+ x_2 \qquad \text{and} \qquad y_4 - \lambda_- x_4 = y_1 - \lambda_- x_1 \tag{3.19}$$

Equation (3.19) will be utilized to calculate the approximate position of the solution point.
Similarly, the compatibility equations (3.17) can be integrated and rearranged to the following relations:

$$(u_2^2 - a_2^2)u_4 + (2u_2v_2 - (u_2^2 - a_2^2)\lambda_+)v_4 = \frac{a_2^2 v_2}{y_2}(x_4 - x_2) + (u_2^2 - a_2^2)u_2 + (2u_2v_2 - (u_2^2 - a_2^2)\lambda_+)v_2 \tag{3.20}$$

and

$$(u_1^2 - a_1^2)u_4 + (2u_1v_1 - (u_1^2 - a_1^2)\lambda_-)v_4 = \frac{a_1^2 v_1}{y_1}(x_4 - x_1) + (u_1^2 - a_1^2)u_1 + (2u_1v_1 - (u_1^2 - a_1^2)\lambda_-)v_1.$$

By solving this four-dimensional equation system for the unknown parameters (x_4, y_4, u_4, v_4), the flow properties of the solution point can be observed. Repeating this process for an increased number of initial points and continuing with the flow properties at the solution points a numerical approximation for the complete supersonic flow field downstream of the initial points can be observed. The resulting network of characteristic lines, including the flow property points, is shown schematically in figure (3.4).

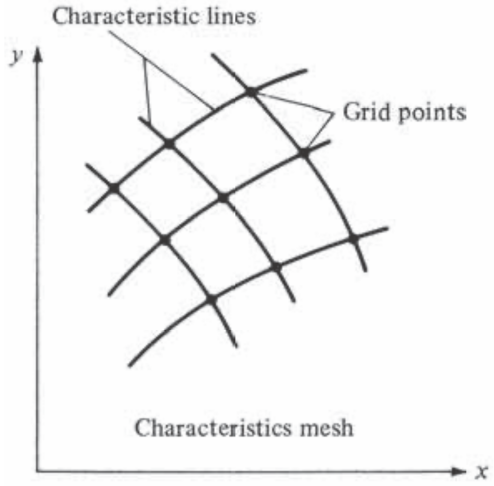

Figure 3.4.: Characteristic mesh for MoC calculation of the supersonic flow field, [3], p.832, Fig. (13.2)

3.2.2. Error minimization

The characteristic lines are mathematical curves, which are linearized into straight sections with the identical initial angle as their characteristic (see figure (3.3)). In order to minimize the resulting linearization error, the initial data points are chosen to be near each other. In addition, an Euler predictor-corrector algorithm is applied [9], [7]. The procedure is as follows:

A predicted solution point $(x_4^p, y_4^p, u_4^p, v_4^p)$ is obtained by evaluating equations (3.19) and (3.20) directly, which corresponds to a first-order Euler integration.

In the subsequent corrector step, the predicted solution is reinserted into the following relations:

$$u_2 = \frac{u_2 + u_4^p}{2} \quad , \quad v_2 = \frac{v_2 + v_4^p}{2} \quad \text{and} \quad y_2 = \frac{y_2 + y_4^p}{2} \tag{3.21}$$

and

$$u_1 = \frac{u_1 + u_4^p}{2} \quad , \quad v_1 = \frac{v_1 + v_4^p}{2} \quad \text{and} \quad y_1 = \frac{y_1 + y_4^p}{2} \tag{3.22}$$

The solutions of the relations (3.21) and (3.22) are then reintroduced into equations (3.19) and, subsequently, with the corrected slopes $\lambda_\pm$, into equations (3.20). This yields a corrected solution point $(x_4^c, y_4^c, u_4^c, v_4^c)$.

Since the predictor and corrector values, in general, do not coincide, the algorithm iterates by taking the corrected state as a new predictor and repeating the process $(k+1)$ times. The iteration is continued until the relative change of the primary flow variables between two consecutive iterations falls below a prescribed tolerance, i.e.

$$\frac{|u_4^{k+1} - u_4^k|}{u_4^k} < \varepsilon \quad , \quad \frac{|v_4^{k+1} - v_4^k|}{v_4^k} < \varepsilon \quad \text{and} \quad \frac{|y_4^{k+1} - y_4^k|}{y_4^k} < \varepsilon \tag{3.23}$$

with ε typically chosen between 10^{-5} and 10^{-6} for engineering accuracy. To prevent infinite correction loops in the event of poor convergence, a maximum number of iterations is set to 10, as recommended in Haberl [10]. In practice, only a few iterations are required for convergence since the predictor step already provides a sufficiently accurate initial estimate. The use of this predictor-corrector approach significantly reduces the accumulation of linearization errors along the characteristic mesh and, therefore, stabilizes the computation of interior points.

3.3. Initial flow condition

As established in section (3.2), the calculation of the flow properties with the MoC requires more than one initial point within the flow field with known properties (x, y, u, v). Since the objective of the method is to obtain the complete supersonic flow regime of the nozzle, the location for prescribing initial conditions is chosen to be the throat. The choking condition at the minimum nozzle area enforces $Ma = 1$, bringing forth initial flow information.

However, when extending the quasi-one-dimensional assumption to two dimensions, the sonic line at the throat cannot be represented as a straight line normal to the principal axis. In an axisymmetric nozzle, the two-dimensional effects introduce a curvature of the sonic line. In 1947, R. Sauer proposed a method to generate this sonic line as a parabola [11]:

$$x = -\frac{(\gamma+1)\left[\frac{2}{(\gamma+1)\rho_t y_t}\right]^{\frac{1}{2}} y^2}{4}, \tag{3.24}$$

where ρ_t and y_t denote the throat curvature radius and the nozzle throat radius, respectively. The resulting Mach line can be viewed in figure (3.5).

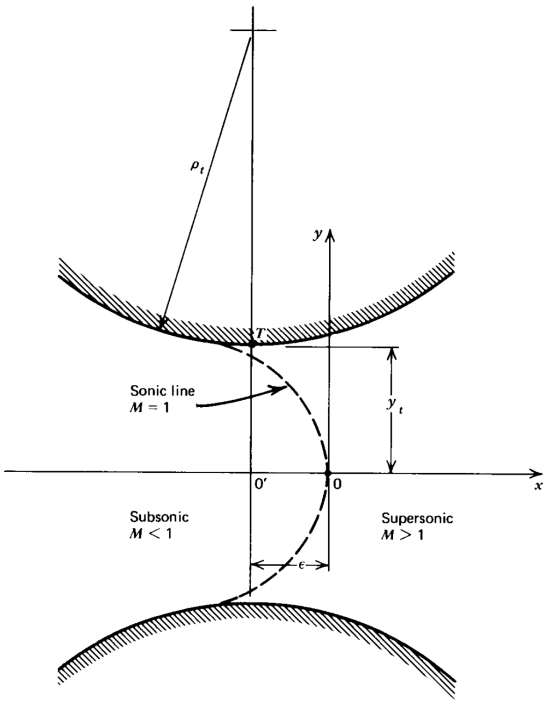

Figure 3.5.: Sonic line at the nozzle throat,[7], p.87, Fig. (15.10)

This parabola, however, poses two problems, as stated in [12]:

Firstly, the Mach line near the wall contour is positioned upstream of the throat, marked as point T in figure (3.5). The flow in this section interferes with the wall contour upstream of point T, which, in this calculation, is not strictly defined. Secondly, as the Mach number of the sonic line is equal to unity, the velocity of the flow equals, by definition, its sonic velocity. Subsequently, the compatibility relations (3.20), derived in section (3.2), are no longer valid, and the generation of a characteristic mesh is impossible.

Therefore, for 2-dimensional, irrotational, axisymmetric flows, a different parabola is proposed as an initial value line (IVL) [12]:

$$x = -\frac{(\gamma+1)\left[\frac{2}{(\gamma+1)\rho_t y_t}\right]^{\frac{1}{2}} y^2}{8} + \epsilon \tag{3.25}$$

with

$$\epsilon = -\frac{(\gamma+1)\left[\frac{2}{(\gamma+1)\rho_t y_t}\right]^{\frac{1}{2}} y_t^2}{8}. \tag{3.26}$$

The correction term ϵ simply ensures that the parabola intersects the nozzle throat at point T as can be seen in figure (3.6). This parabola is defined as a curve holding the flow property $v = 0$ [12] and a constant Mach number.

In theory, the previously mentioned inconsistency of the compatibility equations (3.20) at the throat with the Mach number $Ma = 1$ can be avoided by choosing a Mach number slightly greater than unity. In practice, however, this still poses a problem. For Mach numbers only marginally above one, the associated

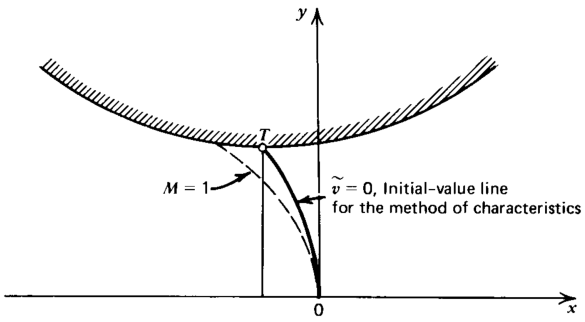

Figure 3.6.: Initial value line at the nozzle throat, [7], p.93, Fig. (15.12)

Mach lines are emitted at angles just below 90°, whereas portions of the IVL parabola exhibit smaller angles. As a result, these Mach lines intersect the parabola and may extend into the subsonic regime, where the relations derived in section (3.1) no longer hold true. To avoid this issue, the Mach number prescribed along the IVL is increased. NozzlePy uses a value of $Ma_{IVL} = 1.1$, which introduces only a minor error that is assumed negligible.

4. Generation of Nozzle Contours

The fundamental principles of axisymmetric, two-dimensional, supersonic flow, derived in chapter (3), are used as the basis for generating nozzle contours, which is discussed in this chapter. After a comparison of different contour generation theories, three contour generation methods and their numerical implementation are presented.

4.1. Assessment of different contour theories

As introduced for a quasi-one-dimensional flow in section (2.3), the geometry in the supersonic region of a nozzle greatly influences the flow properties and, thus, the nozzle performance and resulting thrust. Over the years, several methods for calculating supersonic nozzle geometries have been developed for maximizing nozzle efficiencies and performance. Their concepts and benefits will be discussed in the following:

The ideal contour represents the theoretical baseline for supersonic nozzle design, aiming to produce a perfectly uniform, parallel flow at the nozzle exit with minimal flow disturbances. In this idealized configuration, the static pressure of the exhaust flow at the nozzle exit equals the ambient pressure, ensuring perfectly expanded conditions [1]. To achieve this, the contour is shaped to guide the flow smoothly through a gradual turning process, minimizing deviations from isentropic expansion. This inherently results in a relatively long nozzle geometry, as the flow must be turned over an extended contour length to achieve uniform exit conditions. The required length of the ideal contour is inversely related to the ambient pressure, meaning that for high-altitude or vacuum applications, the nozzle must be significantly elongated to reach equilibrium between the exit and ambient pressures. Consequently, while the ideal contour provides an optimal flow field in theory, its practical implementation is often limited by the resulting structural mass, integration challenges, and diminishing returns in thrust efficiency relative to the added weight and complexity.

In order to minimize these deficits, and at the same time gain the performance benefits of shock-free, ideal expansion, the Truncated Ideal Contour (TIC) method was developed. Its approach is relatively simple: The beforehand calculated ideal contour is truncated at a specific length, allowing a certain loss, as the flow near the wall at the exit plane is neither completely developed nor parallel to the nozzle principal axis. This loss, however, is minimal compared to the benefits of the truncation, which will be discussed in depth in chapter (5).

In 1958, G.V.R. Rao proposed a new method of calculating the nozzle geometry based on the method of characteristics [13]. This approach focuses on the maximization of the nozzle thrust instead of a uniform and parallel flow at its exit plane. Therefore, the initial expansion has a larger maximum wall angle

compared to the ideal contour, while the turning section of the contour has a stronger curvature. A schematic comparison to the TIC contour can be seen in figure (4.1).

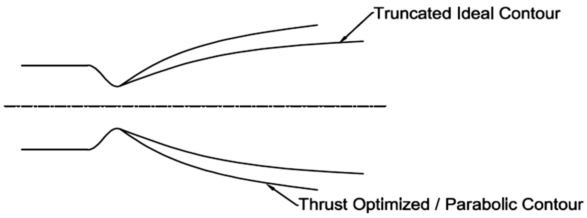

Figure 4.1.: Comparison of TIC and TOP nozzle contour, [1], p.7, Fig. 12

The benefit of this approach is the high area ratio, which originates from the increased initial expansion, which increases the exit Mach number, consequently increasing the thrust of the nozzle as shown in equation (2.15) of section (2.3). In addition, due to the partial compression of the flow at the nozzle wall, the local pressure at the wall near the exit plane is increased, which decreases the problematic recirculation of ambient air at pressure $p_\infty \neq 0$ for atmospheric conditions.

However, the intensified compression in the turning section of the contour inevitably leads to the formation of an oblique shock wave within the supersonic flow field. This phenomenon arises as characteristic lines converge, due to excessive flow turning and local over-compression. Across the shock, entropy increases irreversibly, accompanied by a rise in static pressure and temperature. Simultaneously, the Mach number and flow velocity decrease significantly as part of the total pressure is dissipated into thermal energy. As a consequence, the overall nozzle efficiency is reduced [14]. Such an oblique shock can be observed schematically in figure (4.2). The characteristic lines between the red marked characteristics converge throughout the flow field, thus inducing the internal shock.

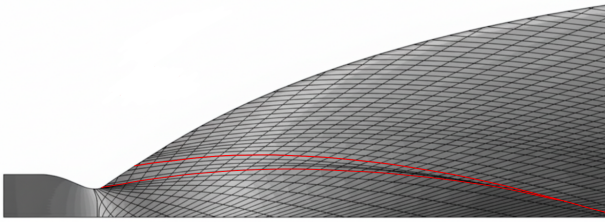

Figure 4.2.: Oblique shock in a typical thrust optimized nozzle, based on [14], p.177, Fig. 4

This thrust optimized contour requires a complete solution of the characteristic mesh, which entails complex numerical programs. Therefore, in 1961, Rao published the Thrust Optimized Parabola (TOP) as an alternative version to his previous approach [15]. The initial nozzle contour can be generated nearly identically by inducing a parabolic curve on a predetermined set of input parameters. This parabola no longer requires the calculation of the supersonic flow field in order to generate a nozzle contour. Since the TOP contour is the far more prevalent nozzle calculation method by Rao, NozzlePy uses only consider this thrust optimized approach.

In 2016, M. Frey et al. introduced a novel approach for generating thrust optimized nozzle geometries without the formation of internal shocks [14]. As illustrated in figure (4.2), the characteristics responsible

for the internal shock of the TOP nozzle originate in a region close to the nozzle throat. The concept of this method, termed TICTOP, involves initiating the expansion with the ideal nozzle contour, thereby preventing shock formation, and subsequently continuing the wall contour using the previously introduced TOP method. Figure (4.3) demonstrates that, following the initial expansion, the characteristic lines no longer converge.

The TICTOP method combines the advantages of relatively high exit pressure, reducing the risk of flow separation, the increased thrust of the TOP contour, and the shock-free expansion typical of the TIC geometry. However, since the benefit of elevated exit pressure near the nozzle wall is negligible for in-space operation, and due to the limited availability of literature on this method, the TICTOP contour will not be considered further in this work.

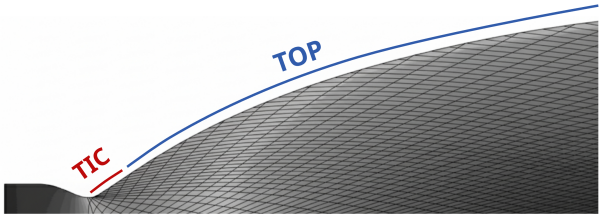

Figure 4.3.: Characteristic mesh of a TICTOP nozzle, based on [14], p. 180, Fig. 11.

For these reasons, the ideal contour, truncated ideal contour, and thrust-optimized parabola will be analyzed and compared in the following.

4.2. Ideal contour

Here, the insight into supersonic flow and its characteristic mesh from chapter (3) will be applied in order to calculate the flow field and, subsequently, the wall contour of an ideal nozzle. An overview of the supersonic flow and its characteristic mesh within an ideal nozzle contour can be observed in figure (4.4). The contour of supersonic nozzles can be divided into two sections: the initial expansion section and, the straightening section. Since the initial expansion section can be somewhat arbitrary [8], it is chosen to be a circular arc with a radius twice that of the nozzle throat. This relatively large initial expansion is justified by Hyde and Gill, [16], who state: '*When the gas density is relatively low (low chamber pressure) or the nozzle is relatively small, the downstream-wall radius ratio R_d/R_t must be large enough to provide expansion slow enough to maintain chemical composition near equilibrium*'. Here, R_d and R_t denote the initial arc radius r_{arc} and throat radius r_t, respectively. This reasoning is consistent with the disregard of chemical kinetic losses in section (5.1).

The calculation of the straightening section, however, requires the complete calculation of the supersonic flow field downstream of the throat.

The characteristic mesh of the ideal contour can be separated into three regions, as defined in figure (4.4). These regions differ significantly regarding the calculation and numerical implementation. The inner region functions as an extension of the initial flow conditions, the middle region describes the reflection

of the Mach lines from the initial expansion wall contour, and the outer region serves to generate the wall contour of the straightening section.

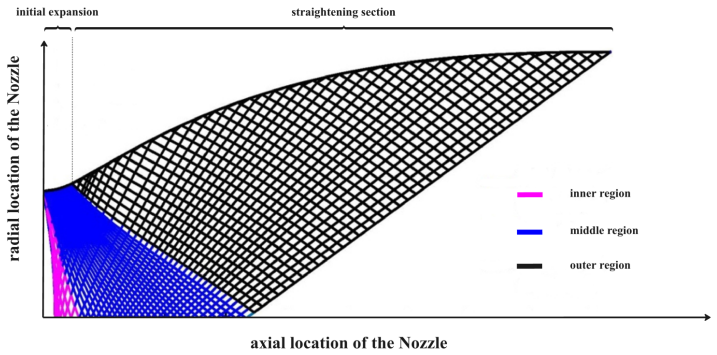

Figure 4.4.: Characteristic mesh of an ideal contour nozzle, based on [17], p. 6033, Fig. 9

4.2.1. Exceptions of point calculation via MoC

The majority of the points calculated for the characteristic mesh follow the linearized MoC, introduced in section (3.2). However, as illustrated in figure (4.4), the characteristic lines reflect off the initial expansion contour wall and, as a consequence of symmetry, off the principal axis of the nozzle (x-Axis).

For the wall contour, this implies that points exist within the flow field that do not originate from both a left- and right-running characteristic, following the MoC as proposed in section (3.2), but only from a left-running characteristic, intersecting with a fixed geometry. Therefore, to gain knowledge of the position and velocity of these points, we can simply substitute both the characteristic and compatibility equations regarding the negative characteristic with the following equations, describing a circular arc:

$$x_4^2 + y_4^2 = r_{arc}^2 \tag{4.1}$$

and

$$\frac{dy_4}{dx_4} = \frac{x_4}{\sqrt{r_{arc}^2 - x_4^2}} = \frac{v_4}{u_4}, \tag{4.2}$$

where r_{arc} denotes the radius of the circular arc at the initial expansion. Combining equations (4.1) and (4.2) with the C_+ equations of (3.19) and (3.20), again, yields a four-dimensional equation system, which exactly defines the unknown variables (x_4, y_4, u_4, v_4) of the characteristic point at the wall. This is done analogously for a fixed parabolic geometry in Zucrow [7].

Similarly, the points positioned directly on the axis of symmetry do not originate from the crossing of a left- and right-running characteristic, but from a C_- characteristic and the symmetry constraint. On the same note, however, the symmetry condition of the flow yields additional information about the regarded point: $y_4 = 0$ and $v_4 = 0$. To calculate the remaining variables x_4 and u_4, the C_- equations of (3.19) and (3.20) are sufficient.

Therefore, every characteristic point in the ideal nozzle flow field can be calculated.

4.2.2. Input parameters

The input parameters for the ideal contour generation tool are presented in Table (4.1). The assigned values are tailored for the S4I2T thruster but can be altered broadly.

It should be noted that the ambient pressure is set to the expected minimum pressure of the vacuum test chamber and will be reduced to $p_\infty = 0$ for the in-space configuration of the thruster.

The resolution of the characteristic mesh is defined by the number of initial characteristic points on the IVL. As stated in the assumptions in section (3.1), the isentropic exponent is chosen to be constant, as it is expected to experience only minimal changes throughout the expansion section of the nozzle, which is further explained in the Appendix (A.1). However, a calculation method for a variable isentropic exponent is presented in [18].

Table 4.1.: Ideal contour generation input parameters

Parameter	**Symbol**	**Value**	**Unit**
Design Mach number at exit plane	Ma_e	$]1.1, 20]$	[-]
Mach number on IVL	Ma_{IVL}	1.1	[-]
Resolution of characteristic mesh	n_l	$[2, \infty)$	[-]
Number of error correction loops	n_e	10	[-]
Error tolerance	ε	10^{-5}	[-]
Combustion chamber pressure	p_{cc}	10^6	$[Pa]$
Ambient pressure	p_∞	320	$[Pa]$
Combustion chamber temperature	T_{cc}	3392	$[K]$
Isentropic exponent	γ	1.12	[-]
Specific gas constant	R	461.52	$[\frac{J}{kgK}]$
Radius of nozzle throat	r_t	0.605	$[mm]$
Radius of circular arc for initial expansion	r_{arc}	1.21	$[mm]$

4.2.3. Initial calculations

At first, the ideal contour generation tool defines the initial value line according to section (3.3) and distributes n_l points equally on the parabola with the values $(x, y, Ma = 1.1, \theta = 0°)$.

Starting with these initial points, the inner characteristic mesh can be determined by the MoC. Numerically, the tool calculates the points originating from the C_- characteristics of the IVL points, starting at the nearest point to the x-Axis and proceeding to the nozzle wall at the throat. Therefore, this algorithm does not consider any characteristic points intersecting with the wall contour. However, since the points positioned on the x-Axis require a different calculation than the inner flow points, a detection of x-Axis points has to take place. As figure (4.5) shows, the index of the points with $y = 0$ is equivalent to $(n^2_{C_-} - 1)$, where n_{C_-} denotes the index of the negative characteristic, originating from the IVL, starting with $n_{(C_-=1)} = 1$. The actual flow points are calculated from the previous point on its characteristic, and the nearest point of the previously calculated characteristic (e.g., point 11 originates from point 10

and point 5 in figure (4.5)). As every initial point on the IVL has the identical Mach number, and no expansion occurs in the inner region, the Mach number and flow angle of the inner region are constant.

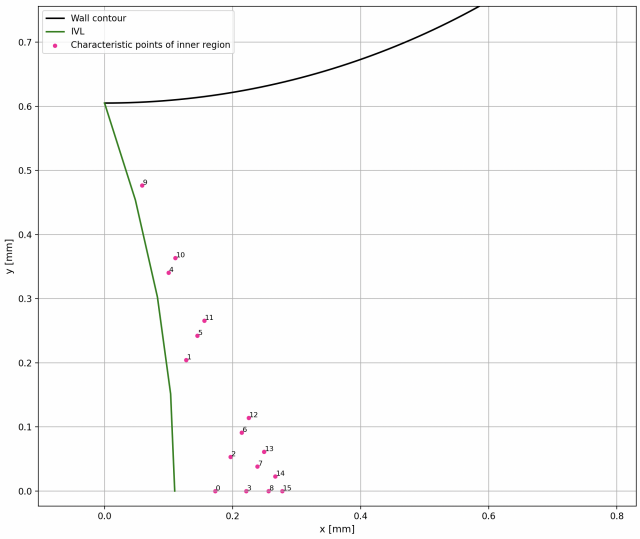

Figure 4.5.: Characteristic points of inner flow region for $n_l = 4$

It should be noted that characteristic points succeeding the points positioned on the x-Axis cannot be calculated by the standard MoC point calculation as well. This occurs as these points emerge from a x-Axis point, with the vertical position $y_2 = 0$. Equation (3.20) for the positive characteristic is no longer defined, as y_2 is in the denominator of the third term. As proposed by Zucrow et al. [7], we simply substitute y_2 and v_2 with y_1 and v_1 for the affected term. The introduced error is dependent on the numerical resolution and can therefore be minimized by increasing the parameter n_l.

4.2.4. Middle region

The middle region requires a more complex algorithm, as it not only reflects an unknown amount of Mach lines at the initial expansion wall contour, but also defines the amount of initial expansion needed for achieving the desired Mach number of the flow Ma_e.

Similar to the inner region, the characteristic points are calculated along their corresponding right-running characteristics, as the point numbers indicate in figure (4.6). Since the MoC derived from the compatibility equations only yields the variables (x, y, u, v), the following relations are in need to gain knowledge of the Mach number and flow angle of the characteristic points:

$$V = \sqrt{u^2 + v^2} \tag{4.3}$$

$$a = \sqrt{\gamma R T_{cc} - \frac{\gamma - 1}{2} V^2}, \tag{4.4}$$

where the definition of the sonic velocity a is based on Zucrow et al. [7]. Subsequently, the Mach number and flow angle can be calculated with:

$$Ma = \frac{V}{a} \tag{4.5}$$

and

$$\theta = \arccos \frac{u}{V}. \tag{4.6}$$

These calculations are appended at every point calculation within the flow field.

The detection of the characteristic points, overlapping the wall contour, is relatively simple, as every point in the middle region with the property $y = 0$ is followed by a wall-contour-point. Therefore, every second characteristic point of each characteristic line determines the next wall reflection point of the following Mach line (e.g., point 80 originating from point 65 in figure (4.6)). The reflection points are calculated as described in the beginning of this section.

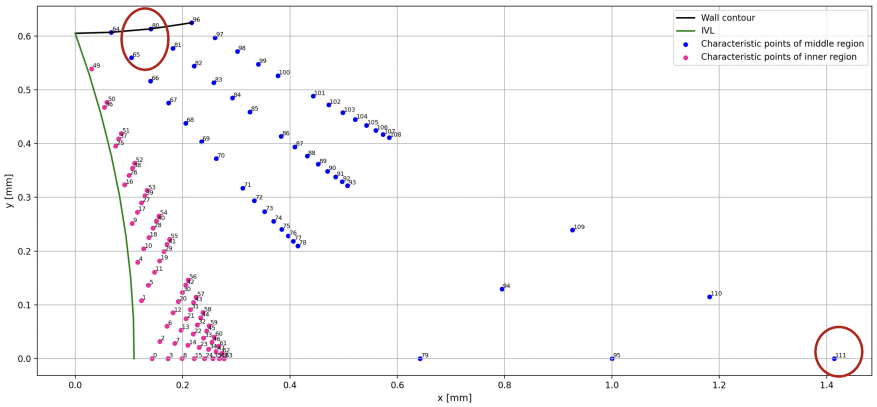

Figure 4.6.: Characteristic points of middle flow region for $n_l = 8$ and $Ma_e = 2$

As previously defined in section (4.1), the ideal contour has a uniform, parallel flow at the nozzle exit. Since the flow angle at the x-Axis and the contour angle at the nozzle exit are both 0 relative to the x-Axis, the flow across the last characteristic of the outer region is uniform and parallel as well. This means that the Mach number along this last characteristic is constant. As shown in figure (4.4), the point of the last C_+ characteristic of the outer region, positioned on the x-Axis, also lies on the last C_- characteristic of the middle region. Since the Mach number at this point is equal to the defined exit Mach number Ma_e, no further expansion of the supersonic flow is needed. The calculation of the characteristic mesh in the middle region is terminated when the Mach number of this point of the last characteristic equals or exceeds Ma_e. In figure (4.6), it is indicated as point 111.

4.2.5. Outer region and turning contour

As there is neither a known geometry, where the characteristic reflects, nor additional crossings of independent characteristic lines, the flow field calculation for the outer region cannot be continued from the last C_- characteristic of the middle region. However, as derived previously, the properties of the supersonic flow at the last characteristic of the nozzle are known. Combined with the characteristic lines of the middle region, the flow field in the outer region can be calculated by inverting the Method of Characteristics:

At first, $(2 \cdot n_l)$ points are evenly distributed along the last characteristic, matching the number of characteristic points positioned on the last middle region characteristic. Thereafter, the MoC is applied by using the points on both linearized Mach lines, which yield a characteristic mesh for the outer region

of the size $(2n_l \times 2n_l)$. In detail, the points of the last- and middle region- characteristic are utilized as the initial points of the C_-- and C_+- characteristic, respectively. The resulting point is positioned upstream of the initial C_- point (e.g. Point 1 in the outer region originates from point 0 on the last characteristic and point 1 of the middle region in figure (4.8)). To now calculate the optimum nozzle contour of the straightening section, we make use of the continuity condition: For a steady flow, the mass flow across each C_- characteristic of the outer region $\dot{m}_{IK_i}$ must be equal to the mass flow across the remaining part of the last characteristic $\dot{m}_{KF_i}$, as indicated by figure (4.7).

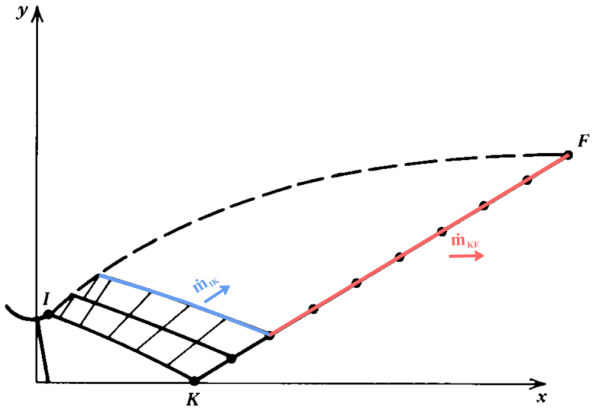

Figure 4.7.: Ideal contour calculation method in the outer flow region, based on Zucrow [7], p.136, Fig. 16.30

To calculate the mass flow at every linearized segment of the characteristics, we use the following relation:

$$\dot{m} = A \cdot \rho \cdot V. \tag{4.7}$$

The area A is approximated to be the lateral surface of a truncated cone with the vertices being the confining characteristic points of the respective segment. The density ρ is calculated by the isentropic equation (2.14), where the total stagnation density ρ_0 resembles the combustion chamber density ρ_{cc}, which is defined by the ideal gas law:

$$\rho_{cc} = \frac{p_{cc}}{R \cdot T_{cc}}. \tag{4.8}$$

Additionally, the velocity vector V is dependent on the angle of the area with respect to the x-Axis. The values for the mass flow of each segment of $\overline{IK}$ are then integrated until the resulting mass flow exceeds the mass flow of the corresponding part of the last characteristic $\dot{m}_{KF}$. The resulting coordinates and flow properties of the two confining characteristic points are then linearly interpolated to match the exact mass flow of the last characteristic. The solution of this interpolation is a contour point of the straightening section. An example of the two points confining the contour point is point 146 and 147 of figure (4.8).

Repeating this process for every C_- characteristic in the outer region yields the resulting nozzle contour. The remaining characteristic points outside of the wall contour are mathematically correct, but resemble no physical solution and can therefore be ignored.

After the resulting contour is exported as a DXF file, the ideal contour program returns the position vectors, as well as the Mach number- and the flow angle-vector of every contour- and flow field-point.

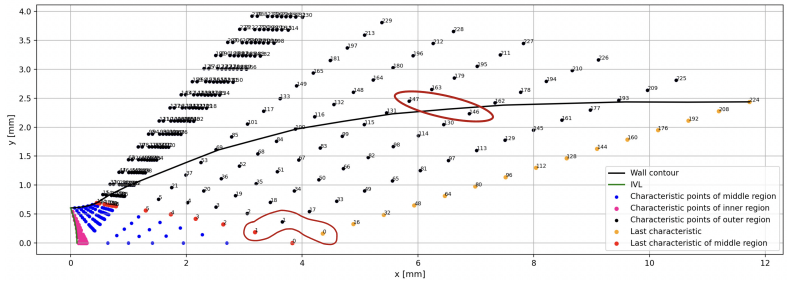

Figure 4.8.: Characteristic points of outer flow region and nozzle contour for $n_l = 8$ and $Ma_e = 3$

This completes the contour generation program for the ideal contour calculation method. A flow chart of the complete algorithm is given in figure (4.9).

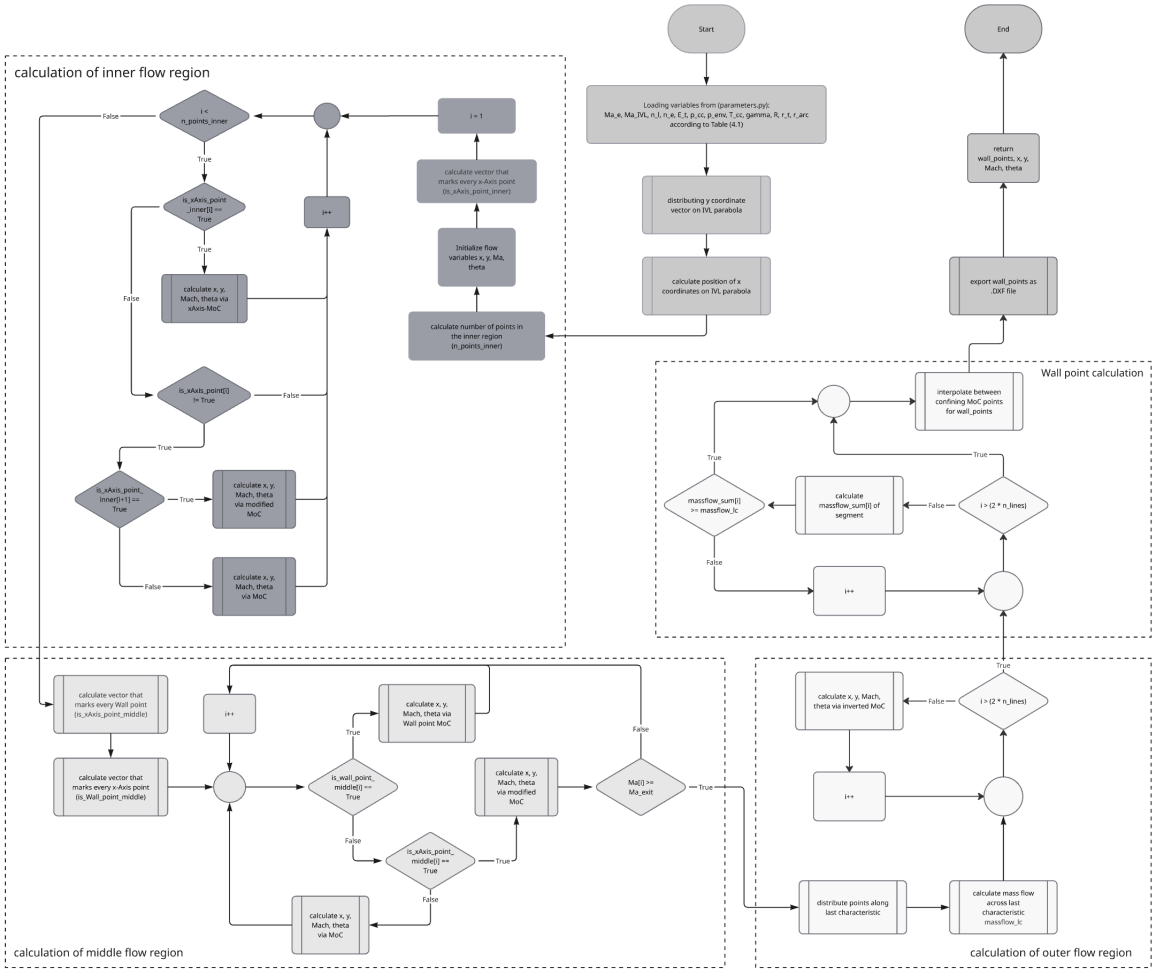

Figure 4.9.: Flow chart of the ideal contour generation algorithm

4.3. Truncated ideal contour

As introduced in section (4.1), the TIC method is based on the ideal contour and simply truncates the nozzle geometry at a specific length. In the following, the numerical implementation of this nozzle contour

generation method will be disclosed.

At first, the TIC program calls up the previously introduced ideal contour method, and the wall contour and flow properties are extracted. Therefore, the ideal contour input parameters, presented in table (4.1) are necessary for the TIC method. In addition, the following input parameters of table (4.2) define the truncation method:

Table 4.2.: TIC generation input parameters

Parameter	Symbol	Value	Unit
Max. nozzle length	l_{max}	False or $]1.21, \infty)$	[mm]
Max. relative nozzle length	l_{rel}	False or $[0.1, 1]$	[-]
Max. nozzle width	w_{max}	False or $]1.815, \infty)$	[mm]
Expansion ratio	ER	False or $[2, \infty)$	[-]
Nozzle contour angle at exit	θ_e	False or $[0, 25_{\pm 10}]$	[°]

These truncation parameters determine, by which method the ideal contour will be cut. Only one input parameter can be given a value; the others must be set to False. One exception to this is the maximum nozzle length l_{max} in combination with the maximum nozzle width w_{max}, which, when both given a value, create a geometric envelope, as shown in figure (4.10).

Each parameter refers to a distinct algorithm, which compares the ideal wall contour coordinates with the given truncation condition. After successful truncation, the resulting contour is again exported as a DXF file. The TIC program, although only processing the contour points, returns the complete flow field alongside the truncated contour, for further investigation into the flow properties at the nozzle exit.

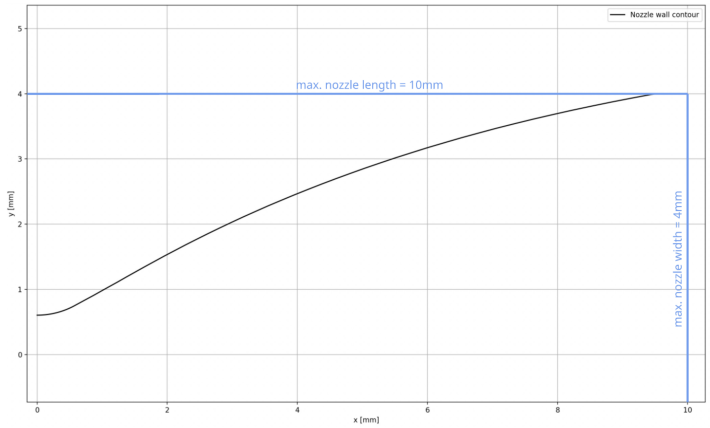

Figure 4.10.: Truncated ideal contour with geometric envelope in blue for $n_l = 40$ and $Ma_e = 4$

Since the ideal contour generation from section (4.2) is an inherent solution of the TIC program for the input parameter $l_{rel} = 1$, the numerical tools developed in the following, will reference the TIC program as the only ideal contour generation software. The TIC algorithm flow chart can be viewed in figure (4.11).

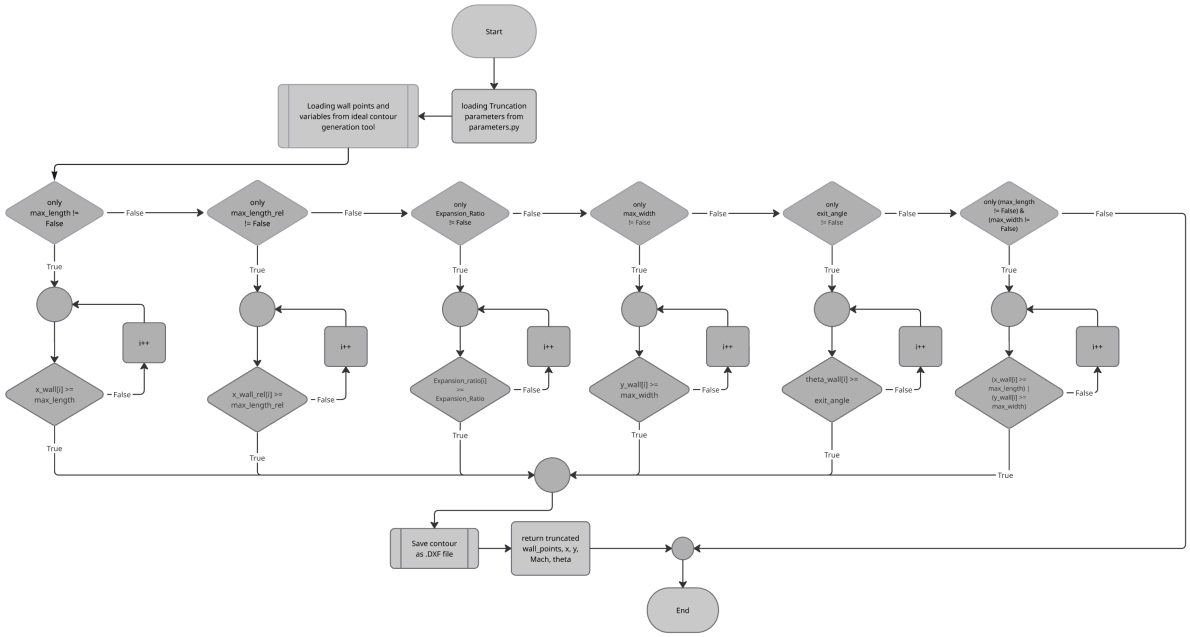

Figure 4.11.: Truncated ideal contour generation algorithm flow chart

4.4. Thrust optimized parabola

The thrust optimized parabola contour is generated by appending a quadratic Bézier curve to an initial expansion contour, consisting of a circular arc [19], [20], which will be discussed in depth in this section.

4.4.1. Input parameters

As the flow properties in the nozzle are irrelevant for the generation of a TOP contour, a new set of input parameters is defined in table (4.3). Although, θ_e and θ_{max} can be set manually, the contour generation utilizes previously calculated values by Rao to match the thrust optimized contour [19]. These parameters depend on a predefined nozzle expansion ratio and nozzle length, as shown in figure (4.12). The nozzle length is defined as the percentage of the length of an equivalent, conically shaped nozzle with the identical expansion ratio. Since the most prevalent TOP contours have a relative length of 80%, it is used for the contour generation tool and no specific input parameter is needed. However, the algorithm developed in section (6), allows for a TOP contour optimization independent of the empirical data by Rao.

4.4.2. Numerical implementation

Firstly, in order to match the input parameters with the parameters required for the data given by Rao, the expansion ratio is calculated using equation (2.15). Similar to the ideal contour, the TOP generation tool then calculates the circular arc points, until the maximum contour angle θ_{max} is reached. The then employed algorithm solves the quadratic Bézier curve graphically, as shown schematically in figure (4.13):

The position and contour angle of Points N and E are known from the input parameters. Following the calculation of the intersection Q of the straights originating from points N and E with the respective angles

Table 4.3.: TOP contour generation input parameters

Parameter	Symbol	Value	Unit
Design Mach number at exit plane	Ma_e	$]2, 20]$	[-]
Max. nozzle contour angle	θ_{max}	$[18, 42]$	[°]
Nozzle contour angle at exit plane	θ_e	$[0, 22]$	[°]
Parabola resolution	res_p	$[2, \infty)$	[-]
Isentropic exponent	γ	1.12	[-]
Radius of nozzle throat	r_t	0.605	$[mm]$
Radius of circular arc for initial expansion	r_{arc}	1.21	$[mm]$

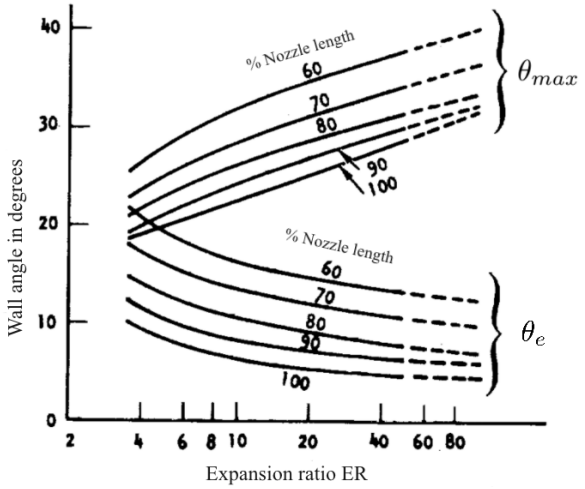

Figure 4.12.: Empirical data for TOP input parameters, based on Hyde et al. [16], p.15, Fig. 5b

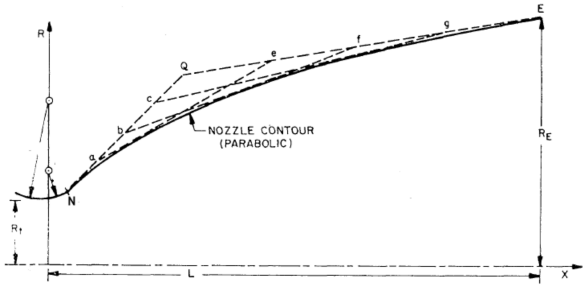

Figure 4.13.: Schematic graphical solution for the TOP contour based on the Bézier curve, Newlands [19], p.3

θ_{max} and θ_e, (res_p) points are distributed evenly along the segments $\overline{NQ}$ and $\overline{QE}$, labeled (a,b,c,e,f,g) in figure (4.13). The contour points of the straightening section of the TOP nozzle are then calculated as intersection points of every two consecutive segments (e.g. $\overline{ae}$ and $\overline{bf}$). The introduced error minimizes with the increase of (res_p). Similar to the previous contour generation methods, the resulting TOP contour is exported as a DXF file and returned as x- and y-coordinate vectors. The exact algorithm is presented in a flow chart in figure (4.14).

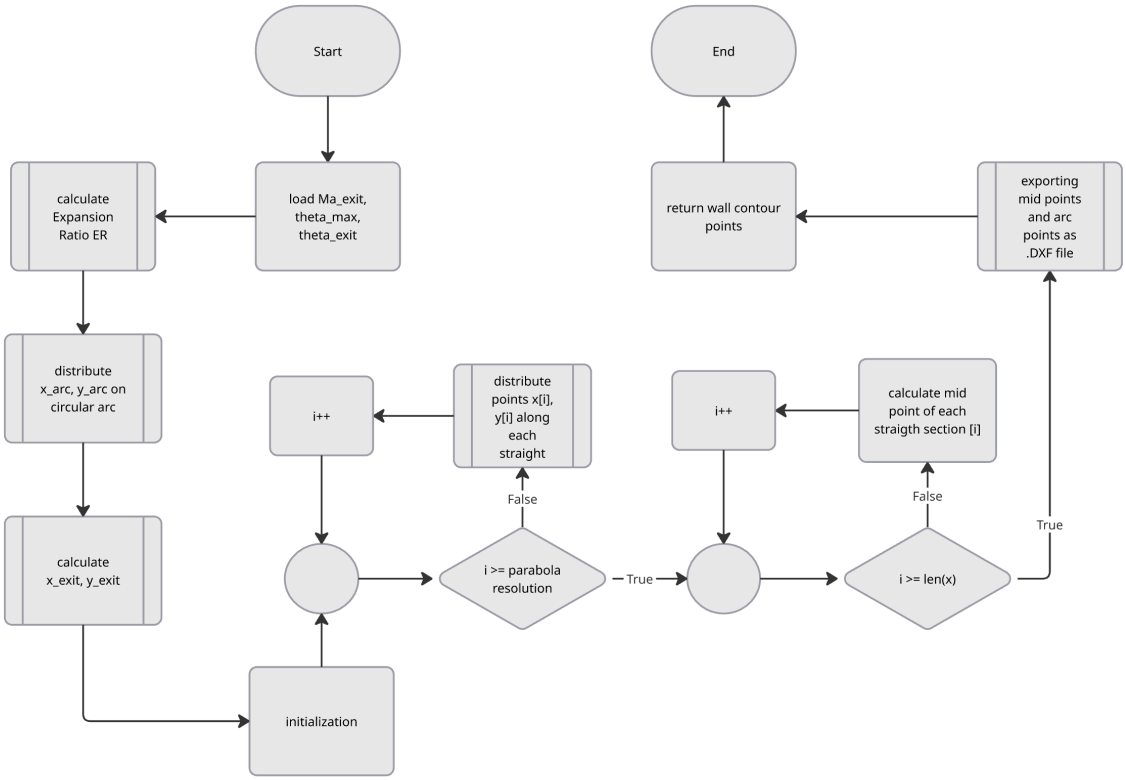

Figure 4.14.: Thrust optimized contour generation algorithm flow chart

5. Investigation of nozzle contour efficiency

To evaluate and compare the performance of different nozzle contours, a detailed understanding of the supersonic flow within the nozzle is essential. This chapter focuses on the analysis of nozzle performance parameters and associated loss mechanisms that influence overall efficiency.

First, the fundamental performance metrics are introduced, followed by a theoretical discussion of the main sources of performance loss. Subsequently, the performance of the TIC and TOP nozzles is analyzed. The numerical methodology used to determine the performance of both configurations is presented in detail. Finally, the influence of the boundary layer on both the geometric contour and the overall performance is discussed. This includes an assessment of how viscous effects alter the effective flow area and contribute to additional performance degradation.

5.1. Nozzle performance parameters and losses

One of the key performance parameters of a rocket engine is its thrust F, which can be determined by the following equation:

$$F = \dot{m}V_e + (p_e - p_\infty)A_e \tag{5.1}$$

It shows that F is greatly dependent on the flow conditions at the exit of the nozzle [21]. As the flow field and geometry of the truncated ideal contour are known, the calculation of the nozzle thrust requires no additional information. However, as elucidated in section (4.4), the TOP calculation yields only the nozzle geometry, without flow information. Therefore, the additional flow information is calculated in section (5.3).

As the thrust directly increases with the size of the combustion chamber, it cannot be utilized as a measurement of the thruster efficiency [22]. Therefore, the specific impulse I_{sp} of a nozzle is introduced, correlating its thrust with the propellant mass flow, as shown in equation (5.2).

$$I_{sp} = \frac{F}{\dot{m} \cdot g_0} \tag{5.2}$$

The constant $g_0 = 9.80665 \frac{m}{s^2}$ denotes the standard gravitational acceleration at Earth's sea level. The specific impulse I_{sp} is a measure of the overall efficiency of a rocket combustion system. However, it inherently depends on the properties of the propellant combination as well as the combustion chamber pressure. The I_{sp} for chemical rocket engines lies between $200s$ and $468s$ [23], which illustrates how significantly the achievable specific impulse varies solely as a result of different propellant combinations.

Therefore, the specific impulse is suitable for comparing the internal performance of nozzles operating with the same propellant mixture and similar chamber conditions; however, it is not appropriate for comparing nozzles designed for different propulsion systems.

In contrast, the thrust coefficient C_f is a dimensionless parameter that measures how effectively the nozzle expands the combusted propellant flow [24]. In this work, it is defined by the following equation:

$$C_f = \frac{F}{p_{cc} \cdot A_t} \tag{5.3}$$

The thrust coefficient characterizes the nozzle performance independently of the propellant's thermochemical characteristics and is thus a more suitable parameter for evaluating and comparing nozzle designs across different propellant combinations.

In accordance with the nozzle efficiency parameters, different performance losses can be derived, which can be categorized into three mechanisms, according to Oestlund, [25]:

- geometric or divergence losses
- viscous drag losses
- chemical kinetic losses

Divergence losses arise from the non-axial direction of the exhaust flow relative to the nozzle axis, leading to a reduction in the effective axial momentum. Viscous drag losses are caused by boundary-layer effects along the nozzle wall, where friction and viscous dissipation decrease the total momentum of the exhaust flow. Since the supersonic flow is assumed to be inviscid (see section (3.1)), this loss mechanism is neglected. However, in section (5.4), we will consider viscosity near the wall contour, which introduces boundary layer losses. Lastly, chemical kinetic losses occur when the chemical reactions within the exhaust gases do not reach equilibrium during the expansion process, resulting in incomplete conversion of thermal energy into kinetic energy. The exhaust gas flow is assumed to be in thermochemical equilibrium downstream of the throat; therefore, chemical kinetic losses are not considered.

5.2. TIC performance analysis

The truncated ideal contour (TIC) introduces two interrelated geometric loss mechanisms.

The truncation of the ideal contour leads to the formation of divergence losses, as illustrated by the velocity profile in Figure (5.1). In contrast to the flow downstream of the last characteristic, the flow at the exit plane near the wall has a radial velocity component, indicating performance loss. However, figure (5.2) shows that the magnitude of these divergence losses, quantified by the Divergence Loss Coefficient C_θ, remains small for low nozzle divergence half-angles. The plot corresponding to the conically shaped simple axisymmetric nozzle provides the closest available approximation to the TIC geometry, although it still overestimates the divergence loss, since the conical flow expansion exhibits greater divergence compared to the partially ideal, initially expanded flow within a TIC nozzle. As indicated in Figure (5.2), for ideal, axisymmetric conical nozzles, a divergence half-angle of 10° results in a performance loss of less

than 1% [26].

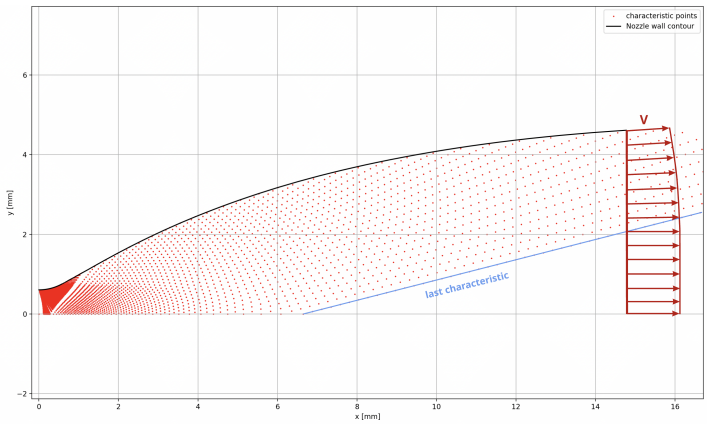

Figure 5.1.: Solution of TIC nozzle with exaggerated velocity profile at exit plane, $n_l = 40$, $Ma_e = 4$, $l_{rel} = 0.6$

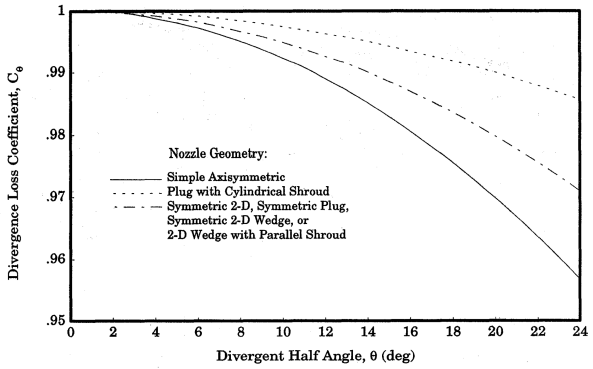

Figure 5.2.: Influence of Divergent Half angle on Divergence Loss for different nozzle geometries, Berton [26], p.16, Fig. 5

In addition to divergence losses, the truncated ideal contour is subject to performance degradation resulting from incomplete expansion. Since the flow expansion is terminated before the exit pressure reaches ambient conditions, the exhaust flow at the nozzle exit remains underexpanded, exhibiting a higher static pressure and a lower velocity than in the corresponding ideal contour. Downstream of the nozzle, the flow continues to expand freely until the ambient pressure is reached; however, this external expansion occurs without wall interaction and, therefore, does not contribute to thrust generation [27]. Consequently, part of the available thermal energy of the gas is not fully converted into axial kinetic energy within the nozzle, leading to a reduction in overall thrust efficiency. This effect, often referred to as incomplete expansion loss or pressure loss, becomes more pronounced as the degree of truncation increases.

In the following, the algorithm developed for determining the performance parameters of a TIC nozzle, as well as the influence of divergence losses on its efficiency, is presented.

The input data for this program is derived from the solution of the TIC contour generation described in section (4.3). Consequently, the parameters listed in Tables (4.1) and (4.2) are required. To compute the nozzle thrust in accordance with equation (5.1), the flow properties at the nozzle exit are extracted.

The flow information of the exhaust gas downstream of the final characteristic line at the exit plane corresponds to that of the last characteristic, as the flow is fully expanded and uniform in this region. However, determining the flow properties of the outer region intersecting the nozzle exit plane requires additional computation. Therefore, the flow variables of the characteristic points enclosing the nozzle exit are linearly interpolated along their axial positions, as illustrated in figure (5.3). The green points indicate the characteristic mesh points near the exit plane, whereas the blue points represent the interpolated exit points. For instance, the fourth point on the exit plane results from the linear interpolation between the confining points 4 and 5.

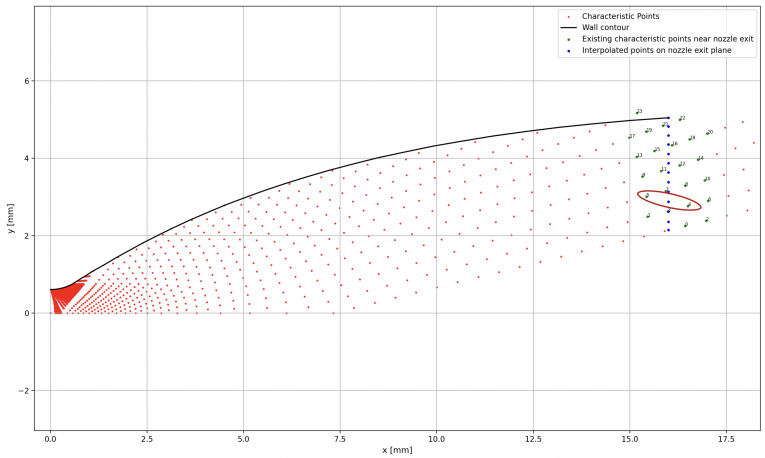

Figure 5.3.: Calculation of flow conditions at nozzle exit for a TIC nozzle, $n_l = 20$, $Ma_e = 4$, $l_{rel} = 0.6$

Accordingly, the thrust is obtained by the following adaptation of equation (5.1):

$$F = \sum_{i}^{n_e} \left[\dot{m}_i V_{e,i} \cos(\theta_i) + (p_{e,i} - p_\infty) A_i \right], \tag{5.4}$$

where n_e denotes the number of discretized points along the exit plane. The partial mass flow $\dot{m}_i$ is computed according to equation (4.7), using the point-specific density ρ_i, the velocity component $V_{e,i} \cdot \cos\theta_i$, and the associated exit area segment A_i.

Analogously, the divergence force is determined by equation (5.5):

$$F_d = \sum_{i}^{n_e} \left[\dot{m}_i V_{e,i} \sin(\theta_i) \right] \tag{5.5}$$

As the divergence force is only affected by axial momentum (see section (5.1)), the pressure term for this force calculation is neglected.

Finally, the specific impulse and thrust coefficient of the nozzle are evaluated according to Equations (5.2) and (5.3).

5.3. TOP performance analysis

As introduced in section (4.1), the loss mechanisms of ideal, inviscid, irrotational, equilibrial flow of a TOP nozzle are the divergence loss and the formation of an oblique shock within the flow field.

In order to calculate the performance as well as the loss mechanisms of such a nozzle, a flow analysis at the exit plane, similar to that of the TIC nozzle, must be performed. Since the TOP contour is generated without conducting a flow field calculation, the exhaust gas properties within the nozzle are unknown. Therefore, a characteristic mesh is generated for the predefined TOP geometry.

5.3.1. Flow field analysis

The characteristic mesh is calculated similarly to that of the ideal nozzle. Therefore, the input parameters for this tool are given in table (4.1). In addition, the geometry of the TOP contour disclosed in section (4.4) is loaded into the program.

Firstly, the initial value line, along with the characteristic mesh of the inner region, is calculated according to the ideal contour generation tool. As the TOP contour provides the nozzle geometry only as a set of wall points, the reflection of the characteristic lines at the initial expansion section can no longer be calculated by the replacement of the C_- characteristic and compatibility equations (3.19) and (3.20) with equations (4.1) and (4.2), defining the geometry of the circular arc. However, a new boundary condition can be set by the defining equations for a point (x_4, y_4) and its derivation (u_4, v_4) on a straight line:

$$\frac{y_4 - y_1}{y_2 - y_1} = \frac{x_4 - x_1}{x_2 - x_1} \tag{5.6}$$

and

$$\frac{dy}{dx} = \frac{y_2 - y_1}{x_2 - x_1} = \frac{v_4}{u_4} \tag{5.7}$$

Employing equations (5.6) and (5.7), in combination with the C_+ equations of (3.19) and (3.20), the unknown position and velocity parameters of a wall point on the TOP contour can be determined. This process is based on the Method of Characteristics for a fixed parabolic geometry in Zucrow et al. [7]. The reflection at the x-Axis is calculated identically to the ideal contour generation program.

The resulting characteristic mesh is shown in figure (5.4).

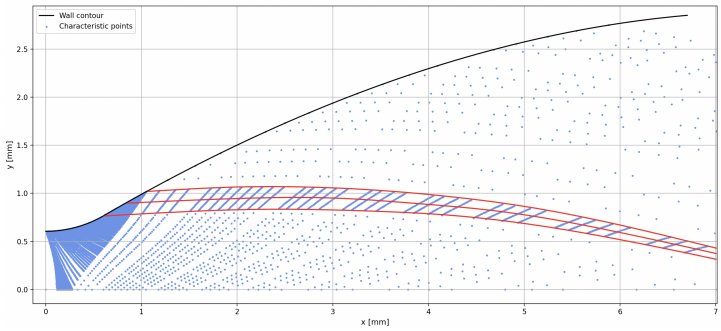

Figure 5.4.: Flow field of TOP nozzle forming an internal oblique shock, $n_l = 40$, $Ma_e = 3.5$, $\theta_{max} = 30°$, $\theta_e = 5°$

Here, the red lines represent the C_- characteristics originating from the first reflection on the straightening section of the TOP contour. As these Mach lines propagate throughout the nozzle, they converge, forming an oblique shock. This behaviour is coherent with the shock wave formation presented in figure (4.2) by Frey, [14]. It should be noted that the converging characteristic lines introduce increased numerical errors, as the linearized characteristic points partially overlap. This effect can be mitigated by increasing the resolution of the characteristic mesh.

5.3.2. Performance calculation

Similar to the performance evaluation of the TIC nozzle, equations (5.1), (5.2), and (5.3) are employed to determine the thrust, specific impulse, and thrust coefficient, respectively. The flow properties at the characteristic points near the nozzle exit plane are linearly interpolated to provide flow information at the exit plane. However, since the flow within the TOP nozzle is neither parallel nor uniform, divergence losses occur across the entire exit plane.

As before, the program outputs the resulting nozzle performance parameters without providing contour or flow field information. The visualization of the performance calculation for the TOP nozzle is presented in figure (5.5).

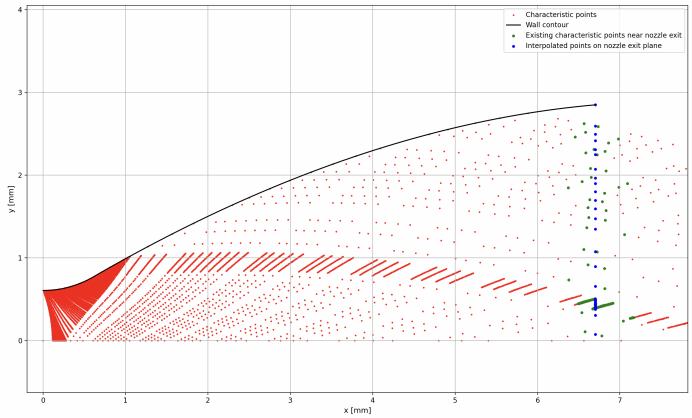

Figure 5.5.: Calculation of flow conditions at the nozzle exit for a TOP nozzle, $n_l = 40$, $Ma_e = 3.5$, $\theta_{max} = 30°$, $\theta_e = 5°$

It should be noted that the flow conditions at each point are computed using the isentropic relations (2.14), (2.16), and (2.17). However, as discussed in section (4.1), an oblique compression shock is associated with a significant increase in entropy. Consequently, the applied method for analyzing the supersonic flow of the TOP nozzle cannot account for the effects of such shock waves. This limitation leads to an overestimation of the TOP nozzle performance.

5.4. Boundary Layer Effects

The performance analysis presented in sections (5.2) and (5.3) accounts solely for geometric losses and neglects viscous effects within the flow. However, for long expansion nozzles commonly employed in spacecraft propulsion systems, the influence of the boundary layer developing along the nozzle wall becomes increasingly significant. This effect is particularly pronounced in small-scale nozzles, where

the relative boundary layer thickness compared to the local flow passage is considerably larger [28]. In such cases, viscous effects result in a reduction of the effective flow area, increased wall friction losses, and deviations from ideal isentropic expansion, thereby decreasing the overall nozzle performance and efficiency. Consequently, in the following analysis, the flow near the nozzle wall is assumed to be viscous.

5.4.1. Boundary layer influence on contour geometry

A fundamental boundary condition for viscous flow along a solid wall is the no-slip condition, which requires the velocity components at the wall to be $u_w = v_w = 0$. The velocity component tangential to the wall contour increases with distance from the wall, as illustrated in Figure (5.6).

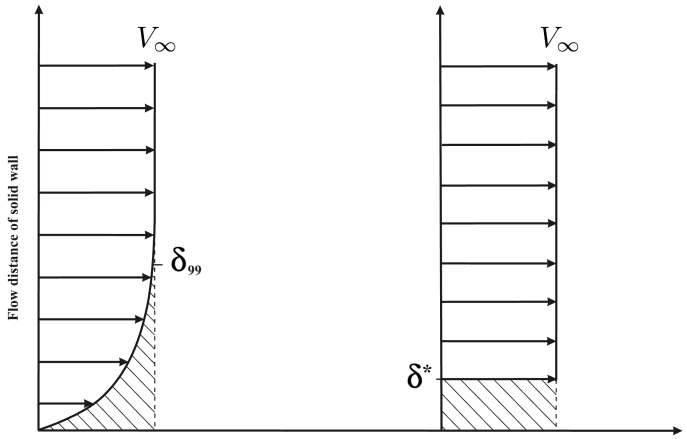

Figure 5.6.: Schematic comparison of Blasius boundary layer δ_{99} and displacement thickness δ^*

Since the velocity asymptotically approaches the freestream velocity V_∞, an exact analytical determination of the boundary layer edge is not computable. A commonly used approximation defines the boundary layer thickness as the distance from the wall at which the local flow velocity reaches 99% of the freestream velocity, denoted by δ_{99}.

However, δ_{99} provides no information about the flow displacement caused by the boundary layer. To account for both the velocity deficit and its influence on the flow displacement, the *Blasius boundary layer displacement thickness*, denoted by δ^*, is introduced [29]. It is expressed by Equation (5.8):

$$\delta^* = 1.72 \frac{s}{\sqrt{Re_s}}, \tag{5.8}$$

where s is the distance along the wall contour, and Re_s is the local, length-based Reynolds number, defined by Equation (5.9):

$$Re_s = \frac{V_\infty s}{\nu}, \tag{5.9}$$

with ν denoting the kinematic viscosity of the flow. The latter can be determined from a modified form of Sutherland's law [30]:

$$\nu = \frac{\mu_0 \frac{T_0+S}{T+S} \left(\frac{T}{T_0}\right)^{\frac{3}{2}}}{\rho}, \tag{5.10}$$

where μ_0 is the reference dynamic viscosity, T_0 the reference temperature, and S the Sutherland constant.

It follows from Equation (5.8) that the displacement thickness δ^* increases progressively along the nozzle contour with increasing s. The velocity within this displacement layer satisfies $V^* = 0$, as the actual integrated velocity of the δ^* layer, equal to the integrated velocity deficit of the freestream outside of δ^*, is added to the freestream velocity (see shaded region in figure (5.6)).

Regarding the characteristic mesh and wall contour determination, Zucrow [7] suggests that the characteristic Mach lines approximately reflect at the Blasius boundary layer. Consequently, in order to preserve the previously calculated inviscid flow field, particularly its shock-free characteristics, the actual wall contour of the viscous nozzle can be obtained by offsetting the ideal inviscid contour by a distance equal to the boundary layer displacement thickness δ^* [7]. The resulting wall contours for both the TIC and TOP nozzles, along with the respective boundary layer displacement thickness distributions, are presented in figures (5.7a) and (5.7b), respectively.

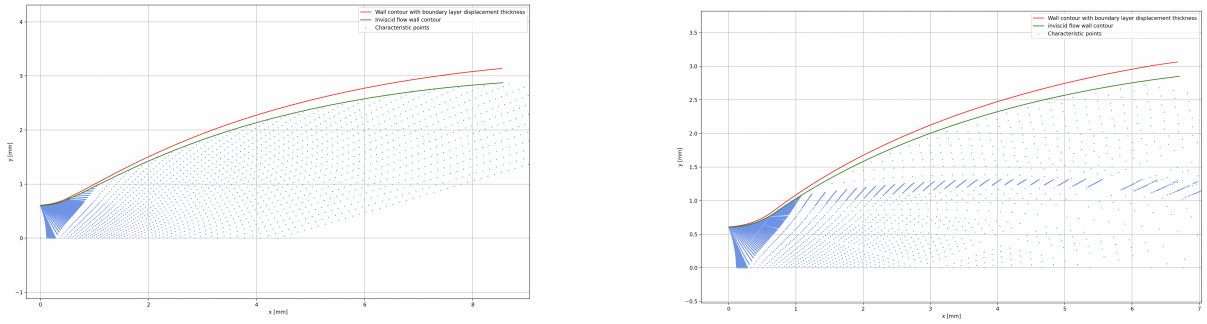

(a) **(b)**

Figure 5.7.: Nozzle contour with boundary layer effects for TIC (a) and TOP (b) for $n_l = 40$, $Ma_e = 3.5$, $l_{rel} = 0.6$, $\theta_{max} = 35°$, $\theta_e = 7°$

5.4.2. Boundary layer performance loss

In order to calculate the performance loss due to the viscous effects of the nozzle flow in the boundary layer, the resulting shear force on the wall must be computed. This is then implemented into the respective nozzle performance calculation algorithm.

Friction on the contour wall induces a local shear stress $\tau_{w,i}$, which, when employing the Blasius boundary layer, can be calculated using the following equations:

$$\tau_{w,i} = \frac{\rho_i}{2} V_{\infty,i}^2 C_{fr,i}, \tag{5.11}$$

where the local friction coefficient $C_{fr,i}$ can be calculated by:

$$C_{fr,i} = \frac{0.664}{\sqrt{Re_{s,i}}} \tag{5.12}$$

Multiplying the local shear stress by the respective area of the nozzle wall segment yields the local shear Force, pointing upstream tangentially to the wall contour. The resulting total shear force F_s parallel to the nozzle principal axis can then be discretely computed by the following sum:

$$F_s = \sum_{i}^{n_w} \tau_{w,i} A_i \cos \theta_{w,i}, \tag{5.13}$$

where n_w denotes the number of wall points, A_i the local contour surface area, and $\theta_{w,i}$ the local wall angle.

This force can then be subtracted from the nozzle thrust, which is subsequently used for the calculation of the specific impulse I_{sp} and thrust coefficient C_f according to section (5.1).

It should be noted that the use of the Blasius boundary layer as a method for calculating both the boundary layer displacement thickness and the shear force is accompanied by a series of approximations.

Firstly, the boundary layer is assumed to be strictly laminar.

An additional assumption of the Blasius boundary layer is that the flow is planar, which does not apply to typical nozzle geometries. The viscous effects on axisymmetric nozzles are inherently smaller than those of planar geometries; therefore, this tool slightly overestimates the boundary layer thickness and shear force.

Lastly, the Blasius boundary layer assumes adiabatic flow with no heat transfer through the nozzle wall. This is presumed throughout every boundary layer calculations.

Therefore, the boundary layer effects discussed in this section are treated as an estimation of the actual effects and are primarily used as a comparison method within the nozzle performance calculation. A shematic overview of the calculation algorithm, used to compute the Nozzle performance is given in figure (5.8).

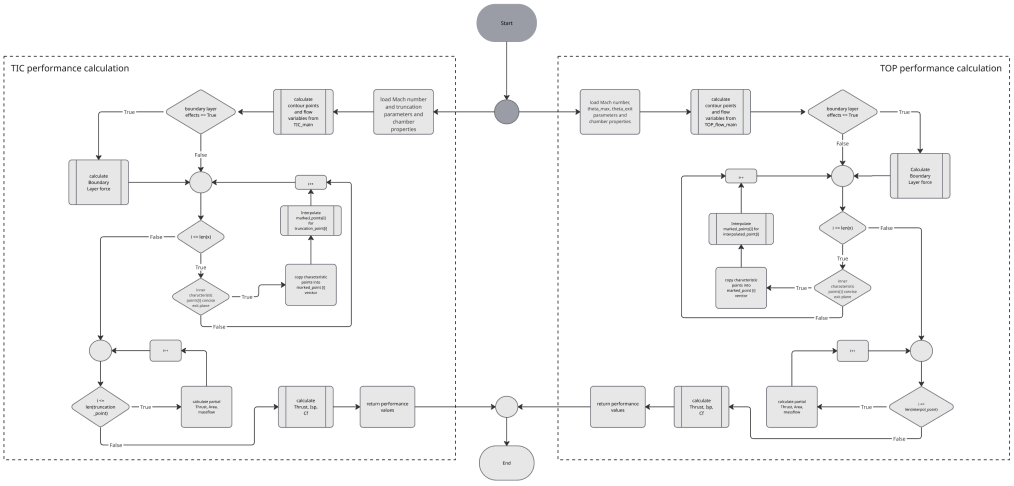

Figure 5.8.: Nozzle performance calculation algorithm flow chart

6. Nozzle performance optimization

The performance of an expansion nozzle for a fixed set of combustion- and flow- parameters still depends on various factors. Therefore, in this chapter, the parameter optimization of the nozzle geometry, based on the calculation of the thrust coefficient C_f from chapter (5), is discussed. Hereby, the input parameters for the TIC nozzle, as well as the TOP contour, presented in tables (4.1), (4.2), and (4.3), will be altered to achieve maximum efficiency.

6.1. Performance optimization TIC nozzles

Since the nozzle throat geometry, as well as the combustion and flow properties of the truncated ideal contour, are defined by external constraints, the optimization parameters for the TIC nozzle are the design Mach number at the exit plane Ma_e and the truncation of the nozzle. In order to ensure the universal applicability of the optimization tool, the relative truncation parameter $l_{max,rel}$ is chosen.

The input parameters for the TIC performance optimization tool are given in table (6.1).

Table 6.1.: Performance optimization input parameters

Parameter	**Symbol**	**Value**	**Unit**
Number of variables per optimization step	n_v	$[2, \infty)$	[-]
Optimization depth	d_{opt}	$[1, \infty)$	[-]

Both the exit Mach number and relative truncation length are initially distributed evenly n_v times across the intervals $[2, 9]$ and $[0.25, 0.9]$, respectively. The optimization tool then loops through the relative truncation length interval for every given Mach number, calculating the thrust coefficient for each contour by employing the performance analysis tool introduced in section (5.2). Once the maximum thrust coefficient is found, the previously calculated optimal contour parameters are overwritten.

However, in order to gain a more detailed optimization without occupying an unnecessary amount of computational power, this initial optimization loop is embedded in an additional loop, which decreases the interval width of the optimal exit Mach number and truncation length, respectively. This algorithm, therefore, locally increases the resolution of the previously calculated maximum nozzle parameters. A schematic overview of this optimization mechanism is given in figure (6.1).

As the TIC optimization is complete, the thrust coefficient, exit Mach number, and relative truncation length are displayed and can then be employed in the TIC generation tool presented in section (4.3) in order to export the optimal TIC nozzle geometry.

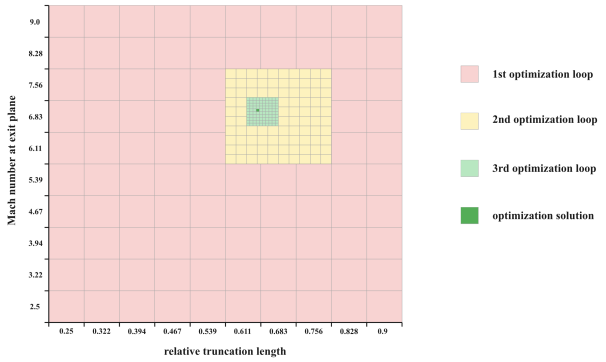

Figure 6.1.: Schematic of the optimization logic for a truncated ideal nozzle, $n_v = 10$, $d_{opt} = 3$

6.2. Performance optimization TOP nozzles

The optimization of the TOP nozzle is performed analogously to the procedure described in section (6.1). The corresponding input parameters are listed in table (6.1).

As introduced in section (4.4), the TOP contour geometry, designed to have a length equivalent to that of an 80% conical nozzle, is defined by the parameters θ_{max} and θ_e. Iterating over these variables and subsequently solving the characteristic mesh of the supersonic flow field yields the optimal TOP nozzle contour.

However, to determine the global optimum of the TOP nozzle geometry, the nozzle length and, consequently, its expansion ratio must also be varied. By applying the area–Mach number relation given in Equation (2.15), the exit Mach number Ma_e can be used as an equivalent design variable. With this additional parameter, the optimization logic deviates from that of the TIC optimization.

Typical variation ranges for the maximum wall angle, exit angle, and exit Mach number are $[18, 42]$, $[2, 22]$, and $[2, 9]$, respectively. The core optimization algorithm comprises three nested primary loops, which iterate through these θ_{max}, θ_e, and Ma_e intervals. Similar to the TIC optimization, an additional adaptive loop refines the parameter ranges based on the previously obtained maximum nozzle performance. The resulting optimal TOP nozzle parameters are subsequently displayed and can be directly implemented in the TOP contour generation tool introduced in section (4.4).

As the accuracy of the optimization results strongly depends on the resolution of the characteristic mesh, this efficient optimization algorithm enables the calculation of the flow field with increased level of detail. The implementation logic for the optimization tool for both nozzle generation methods can be seen in figure (6.2).

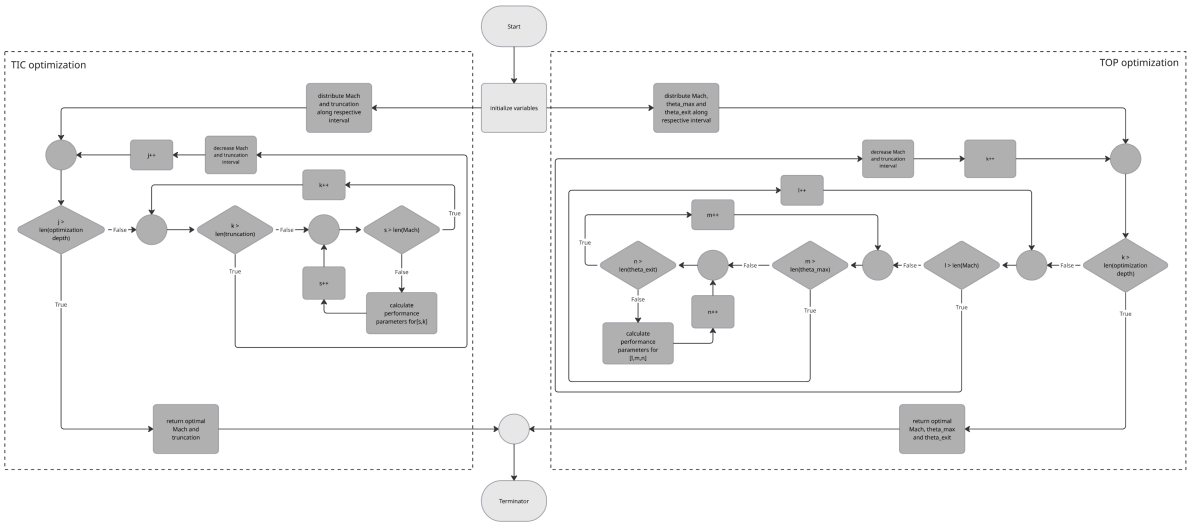

Figure 6.2.: Nozzle optimization algorithm flow chart

Bibliography

[1] S. Khare and U. K. Saha, "Rocket nozzles: 75 years of research and development," *Sādhanā – Academy Proceedings in Engineering Sciences*, vol. 46, pp. 1–7, 2021. [Online]. Available: https://doi.org/10.1007/s12046-021-01584-6Sadhana(0123456789().,-volV)FT3%5D(012345%206789().,-volV) (cit. on pp. 1, 16, 17).

[2] "Nozzle de laval diagram," Accessed: 2025-10-14. [Online]. Available: https://en.wikipedia.org/wiki/De_Laval_nozzle#/media/File:Nozzle_de_Laval_diagram.svg (cit. on p. 1).

[3] J. Anderson John D., *Fundamentals of aerodynamics*, 6th ed. McGraw-Hill Higher Education, 2011, ISBN: 978-1-259-12991-9. [Online]. Available: http://lccn.loc.gov/2015040997 (cit. on pp. 3, 4, 12).

[4] H. Fischer and H. Kaul, *Mathematik für Physiker. Band 2: Gewöhnliche und partielle Differentialgleichungen, mathematische Grundlagen der Quantenmechanik*, 4th updated edition. Springer Spektrum, 2014, p. 198, ISBN: 978-3-658-00476-7. [Online]. Available: https://doi.org/10.1007/978-3-658-00477-4 (cit. on p. 7).

[5] S. W. Wolf, "Supersonic wind tunnel nozzles: A selected, annotated bibliography to aid in the development of quiet wind tunnel technology," Tech. Rep., 1990, pp. 1–2. [Online]. Available: https://ntrs.nasa.gov/citations/19900016703 (cit. on p. 7).

[6] M. J. Zucrow and J. D. Hoffman, *Gas Dynamics, Multidimensional Flow*. Malabar, Florida: Robert E. Krieger Publishing Company, 1976, vol. 1, ISBN: 978-0-89874-840-6 (cit. on pp. 7, 9, 11).

[7] M. J. Zucrow and J. D. Hoffman, *Gas Dynamics, Multidimensional Flow*. Malabar, Florida: Robert E. Krieger Publishing Company, 1976, vol. 2, ISBN: 978-0-89874-840-6 (cit. on pp. 7, 12, 14, 15, 19, 21, 23, 33, 36).

[8] J. Anderson John D., *Modern Compressible Flow: With Historical Perspective* (McGraw-Hill Series in Aeronautical and Aerospace Engineering), 3rd ed. New York, NY: McGraw-Hill Higher Education, 2003, pp. 390, 397, 401, International edition: ISBN 0-07-112161-7, ISBN: 0-07-242443-5 (cit. on pp. 9, 10, 18).

[9] R. L. Malig, "Comparision of predictor-corrector methods," M.S. thesis, Naval Postgraduate School, Monterey, California, 1972, pp. 28–36 (cit. on p. 12).

[10] D. Haberl, "Design and characterization of axisymmetric expansion-deflection nozzles for high-altitude applications," Supervisors: Prof. Dr.-Ing. Chiara Manfletti, Dr.-Ing. Manuel Frey, Dipl.-Ing. Thomas Aichner, Master's Thesis, Technical University of Munich, 2024, p. 32 (cit. on p. 13).

[11] R. Sauer, "General characteristics of the flow through nozzles at near critical speeds," National Advisory Committee for Aeronautics (NACA), Washington, D.C., Tech. Rep. Technical Memorandum 1147, 1947, Translated from: Allgemeine Eigenschaften der Strömung durch Düsen in der Nähe der kritischen Geschwindigkeit, Deutsche Luftfahrtforschung, Forschungsbericht Nr. 1992, Berlin-Adlershof, Sept. 25, 1944 (cit. on p. 13).

[12] R. Gioia, "Method of characteristics to design symmetric and asymmetric converging-diverging nozzles for real gas applications," Advisor: Prof. Alessandro Romei; Co-advisor: Dr. Noraiz Mushtaq, Master's Thesis, Politecnico di Milano, Milan, Italy, 2023, pp. 19–25 (cit. on p. 14).

[13] G. V. R. Rao, "Exhaust nozzle contour for optimum thrust," *Jet Propulsion*, vol. 28, no. 6, pp. 377–382, 1958 (cit. on p. 16).

[14] M. Frey, K. Makowka, and T. Aichner, "The tictop nozzle: A new nozzle contouring concept," *CEAS Space Journal*, vol. 9, no. 2, pp. 175–181, 2016 (cit. on pp. 17, 18, 34).

[15] G. V. R. Rao, "Recent developments in rocket nozzle configurations," *ARS Journal*, vol. 31, no. 11, pp. 1488–1491, 1961 (cit. on p. 17).

[16] J. C. Hyde and G. S. Gill, "Liquid rocket engine nozzles," National Aeronautics and Space Administration (NASA), Lewis Research Center, Cleveland, Ohio, Tech. Rep. NASA SP-8120, Jul. 1976, Prepared under the direction of Howard W. Douglass; project management by Harold Schmidt; edited by Russell B. Keller, Jr. [Online]. Available: `https://ntrs.nasa.gov/archive/nasa/casi.ntrs.nasa.gov/19760023255.pdf` (cit. on pp. 18, 27).

[17] K. Rafiq, M. Rasheed, M. M. Afzal, and J. H. Masoodi, "Influence of ideal nozzle geometry on supersonic flow using the method of characteristics," *Journal of Mechanical Science and Technology*, vol. 36, no. 12, pp. 6027–6039, 2022. [Online]. Available: `http://doi.org/10.1007/s12206-022-1118-2` (cit. on p. 19).

[18] D. Sun, T. Luo, and Q. Feng, "New contour design method for rocket nozzle of large area ratio," *International Journal of Aerospace Engineering*, vol. 2019, pp. 1–8, 2019. [Online]. Available: `https://doi.org/10.1155/2019/4926413` (cit. on p. 20).

[19] R. Newlands, "The thrust optimised parabolic nozzle," Hybrid Effects Technical Papers, Tech. Rep., 2017, Updated: 18 April 2017. [Online]. Available: `https://www.hybrideffects.com/technical-papers/` (cit. on pp. 26, 27).

[20] J. P. C. Silva and F. Brójo, "A review on supersonic nozzle design and analysis with traditional methods," *Preprints*, pp. 51–53, 2025, Preprint, not peer-reviewed. [Online]. Available: `https://doi.org/10.20944/preprints202503.1464.v1` (cit. on p. 26).

[21] T. Fernandes, A. Souza, and F. Afonso, "A shape design optimization methodology based on the method of characteristics for rocket nozzles," *CEAS Space Journal*, vol. 15, no. 3, p. 873, 2023. [Online]. Available: `https://doi.org/10.1007/s12567-023-00511-1` (cit. on p. 29).

[22] R. Zucker and O. Biblarz, *Fundamentals of Gas Dynamics*, 2nd. Hoboken, New Jersey: John Wiley & Sons, 2002, p. 382, ISBN: 978-0-471-05994-8 (cit. on p. 29).

[23] G. P. Sutton and O. Biblarz, *Rocket Propulsion Elements*, 9th. Hoboken, New Jersey: John Wiley & Sons, 2017, p. 30, ISBN: 9781118753651. [Online]. Available: `https://www.wiley.com/en-us/Rocket+Propulsion+Elements%2C+9th+Edition-p-9781118753651` (cit. on p. 29).

[24] D. K. Huzel and D. H. Huang, *Modern Engineering for Design of Liquid-Propellant Rocket Engines* (Progress in Astronautics and Aeronautics), Revised, updated, and enlarged, H. Arbit et al., Eds. Washington, D.C.: American Institute of Aeronautics and Astronautics, 1967, vol. 147, pp. 11–12, ISBN: 1-56347-013-6. [Online]. Available: https://ntrs.nasa.gov/citations/19710019929 (cit. on p. 30).

[25] J. Östlund, "Flow processes in rocket engine nozzles with focus on flow separation and side-loads," TRITA-MEK Technical Report 2002:09, ISSN 0348-467X, ISRN KTH/MEK/TR–02/09-SE, Licentiate Thesis, Royal Institute of Technology (KTH), Department of Mechanics, Stockholm, Sweden, 2002, p. 9 (cit. on p. 30).

[26] J. J. Berton, "Divergence thrust loss calculations for convergent-divergent nozzles: Extensions to the classical case," National Aeronautics and Space Administration (NASA), Lewis Research Center, Cleveland, Ohio, Tech. Rep. NASA TM-105176, Aug. 1991, NASA Technical Memorandum. [Online]. Available: https://ntrs.nasa.gov/citations/19910012722 (cit. on p. 31).

[27] E. Priambodo, *Nozzle design theory*, *Design and Analysis of Rocket Nozzle*, Chapter 2, 2010. [Online]. Available: https://digilib.itb.ac.id/assets/files/disk1/368/jbptitbpp-gdl-ekopriamad-18355-3-2010ta-2.pdf (cit. on p. 31).

[28] T. W. Gerhold, "Performance study of post-processed additively manufactured low thrust nozzles," Master's Thesis, Air Force Institute of Technology (AFIT), Wright-Patterson Air Force Base, Ohio, 2022, p. 1. [Online]. Available: https://apps.dtic.mil/sti/citations/AD1178690 (cit. on p. 35).

[29] H. Schlichting and K. Gersten, *Boundary-Layer Theory*, 9th. Berlin, Germany: Springer-Verlag Berlin Heidelberg, 2017, ISBN: 978-3-662-52918-4. [Online]. Available: https://doi.org/10.1007/978-3-662-52919-1 (cit. on p. 35).

[30] "Sutherland's law." based on Values from F.M.White, Viscous Fluid Flow, 3rd ed., McGraw-Hill, 2006, Accessed: 2025-10-13. [Online]. Available: https://doc.comsol.com/5.5/doc/com.comsol.help.cfd/cfd_ug_fluidflow_high_mach.08.27.html (cit. on p. 35).

[31] S. Gordon and B. J. McBride, "Computer program for calculation of complex chemical equilibrium compositions and applications, part i: Analysis," NASA, Cleveland, Ohio, Tech. Rep. NASA RP-1311, 1994, NASA Reference Publication 1311 (cit. on p. 44).

A. Appendix

A.1. CEA results

In the following table, the solution of quasi-one-dimensional chemical equilibrium calculations, for the initial flow conditions of the S4I2T combustion chamber is presented. The values are computed by the software NASA CEA [31].

Table A.1.: Flow properties from NASA CEA

A/A_t	γ	Mach
Chamber	1.1303	0
1	1.1254	1
3	1.1105	2.310
10	1.1023	3.045
20	1.0989	3.412
30	1.0973	3.616
50	1.0956	3.865
80	1.0944	4.089
100	1.0940	4.193
150	1.0935	4.380
200	1.0934	4.511
300	1.0936	4.695
400	1.0942	4.824

This solution shows that the isentropic exponent γ changes only marginally throughout the expansion nozzle and justifies the assumption of ($\gamma = const.$).